Reviews of Modern Plasma Physics (2019) 3:3
https://doi.org/10.1007/s41614-019-0024-2

TOPICAL COLLECTION: REVIEW PAPER

Recent Progress in Physics of Plasma-Based Space Propulsion

Helicon-type radiofrequency plasma thrusters and magnetic plasma nozzles

Kazunori Takahashi[1]

Received: 6 January 2019 / Accepted: 28 April 2019 / Published online: 22 May 2019

Abstract

Development of electrodeless radiofrequency plasma thrusters, e.g., a helicon thruster, has been one the of challenging topics for future high-power and long-lived electric propulsion systems. The concept simply has a radiofrequency plasma production/heating source and a magnetic nozzle, while it seems to include many aspects of physics and engineering issues. The plasma produced inside the source is transported along the magnetic field lines and expands in the magnetic nozzle, where the plasma is spontaneously accelerated into the axial direction along the magnetic nozzle, yielding a generation of the thrust force. Hence, the plasma transport and spontaneous acceleration phenomena in the magnetic nozzle are key issues to improve the performance of the thrusters. Since the thrust is equal in magnitude and opposite in direction to momentum flux exhausted from the system, the direct measurement of the thrust can reveal not only the thruster performance but also fundamental physical quantity of plasma momentum flux. Here studies on fundamental physics relating to the thruster development and the technology for the compact and efficient system are reviewed; the current status of the thruster performance is shown. Finally, a recently proposed future new application of the thruster is also discussed.

Keywords Helicon thruster · Magnetic nozzle · Electrodeless plasma thruster · Plasma expansion · Plasma momentum

1 Introduction

Over the past few decades various types of electric propulsion devices have been developed and successfully utilized in space missions, e.g., ion-gridded thrusters in DEEP-SPACE 1 (Brophy 2002) and HAYABUSA/MUSES-C missions (Kuninaka et al. 2006), a Hall thruster in SMART 1 (Koppel et al. 2005) mission, and so on.

✉ Kazunori Takahashi
kazunori@ecei.tohoku.ac.jp

[1] Department of Electrical Engineering, Tohoku University, Sendai 980-8579, Japan

Representative important parameters showing the propulsion performance are a thrust F, a specific impulse I_{sp}, and a thruster efficiency η, where the latter two can be given as

$$I_{sp} = \frac{F}{\dot{m}g}, \tag{1}$$

$$\eta = \frac{F^2}{2\dot{m}P}, \tag{2}$$

with the mass flow rate $\dot{m}$ of the propellant gas, the gravitational acceleration g, and the electric power P. Since the ionized propellant is accelerated via hydrodynamic, electrostatic, and electromagnetic acceleration processes induced by an electric power obtained in space, the electric power can be converted into the material momentum in the electric propulsion devices, yielding higher specific impulse and reducing the propellant mass mounted on the system. Hence the dynamics of the ionized gas, i.e., the plasmas, significantly affect the thruster performance. As seen in Eqs. (1) and (2), the specific impulse I_{sp} and the thruster efficiency η can be assessed by measuring the thrust force F with the given mass flow rate $\dot{m}$ of the propellant and the electric power P. Therefore, the direct measurement of the thrust is the most important experimental issue for the thruster assessment.

The thrust force F in Fig. 1a is equal in magnitude and opposite in direction to the momentum exhausted from the system per unit time, corresponding to sum of static (nk_BTA) and dynamic (mnv^2A) pressures for fluid having a density n, a temperature T, a mass m of particles forming the fluid, a mean velocity v, and a cross section A of the fluid flow. Hence the thrust force can be in principle obtained by measuring the density, temperature, velocity, and their spatial profiles. In the field of plasma physics, a large number of studies for the measurements of the density, temperature, and velocity have been performed for the last several decades. In addition to these quantities averaged in the velocity space, some diagnostics can reveal the detailed

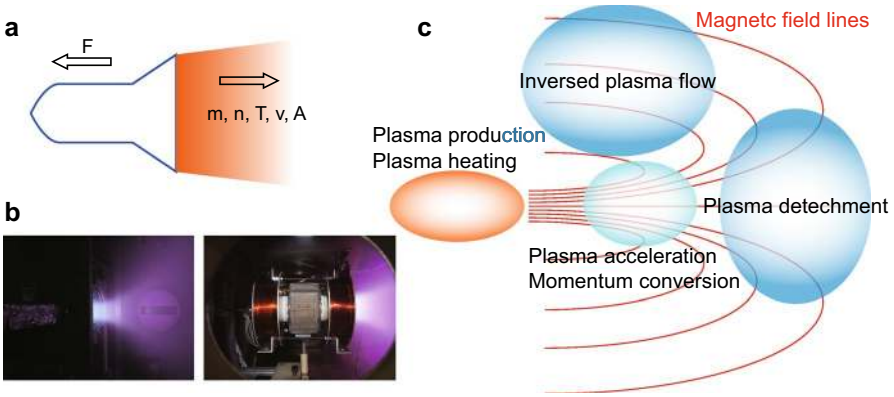

Fig. 1 **a** Physical picture of the thrust imparted by the momentum flux exhausted from the rocket. **b** Typical photographs of the helicon thrusters operated at the Australian National University and Tohoku University. **c** Physical issues in the rf magnetic nozzle plasma thrusters

energy/velocity distributions of the charged particles. These can give many insights into the plasma physics relating to the thruster development. However measurements of reliable absolute values of these physical quantities require great effort to calibrate the diagnoses, even in the well-known Langmuir probe techniques, e.g., due to a sheath expansion effect around the Langmuir probe (Sheridan 2000). Thrust stands often used in the electric propulsion community can give the absolute value of the force exerted to the thruster structure (Xu and Walker 2009), i.e., the absolute value of the total momentum flux exhausted from the system. This is the spatially integrated value and cannot give the local physical quantities, while the combination of the thrust measurement technique and the plasma diagnostics give great insight into not only the thruster assessment but also the physics underlying the thruster development as described later.

The thrusters can be roughly classified by the plasma production and/or acceleration mechanisms, e.g., DC arcjet (Martinez-Sanchez and Pollard 1998), magnetoplasmadynamic (MPD) thrusters (Kuriki and Inutake 1974; Sasoh 1994; Zuin et al. 2004), ion gridded thrusters (Snyder et al. 2012), and Hall thrusters (Diamant et al. 2006). Most of these mature electric propulsion devices include electrodes exposed to the plasmas for plasma production or acceleration, where sputtering due to incident ions to the electrodes or erosion due to spots of electric current induce damages of the electrodes; the lifetime of the propulsion device is actually limited. This problem is expected to become more conspicuous when operating it with high electric power. For propulsion devices that are used over a long period and for a high power, electrodeless plasma thruster have been studied as alternative and innovative options but are extremely challenging topics. When no electrode is exposed to the plasma, the electric power has to be transferred to the plasma via a radiofrequency (rf) heating or a microwave heating; the system inevitably has zero net current, i.e., is 'current-free'. Even in inductively-coupled or wave-coupled rf plasma sources, the rf high voltage at the antenna strap is capacitively coupled with the plasma and induces wall charging phenomenon, which creates the strong electric field accelerating the ions to the wall inner surface and the resultant physical etching of the dielectric wall (Berisford et al. 2010). However a Faraday shield would be useful to inhibit the capacitive coupling and to extend the lifetime of the source (Hoopwood 1992).

When the flux of the ions exhausted from the spacecraft is unbalanced with that of the electrons, the spacecraft is immediately charged up and the exhausted ions are pulled back to the spacecraft by the self-induced electric field. Therefore, fluxes of the positive and negative charges exhausted from the spacecraft have to be equal, i.e., the net current exhausted from the spacecraft (defined as *global current*) has to be zero, which is common for all the electric propulsion devices. Hence neutralizers exhausting electrons have to be mounted on the electrostatic plasma thruster such as the ion-gridded and Hall thrusters to sustain the zero global current. Since the light electrons can follow the accelerated ions, the charge balance in the plume can be sustained. The condition of the zero global current is mandatorily sustained in the rf 'current-free' plasma thrusters. Some concepts of the current-free plasma thrusters are described in the Sect. 2 of 'Radiofrequency magnetic nozzle plasma thruster', most of which utilize plasma dynamics in an expanding magnetic field called a magnetic nozzle, where typical photographs of the rf magnetic nozzle plasma thrusters

indicating the magnetic plasma expansion are seen in Fig. 1b. In this type of the thrusters, various processes of the plasma acceleration and the momentum conversion can occur simultaneously with the magnetic expansion as sketched in Fig. 1c. Furthermore, many aspects of physics are still unclear, e.g., a plasma detachment from the magnetic nozzle. Diagnostics of the plasma, the thrust, and the momentum flux, are important to investigate the plasma dynamics and mentioned in the Sect. 3 of 'Diagnostics of plasmas and thrusters'. This review then focuses on physics and technologies of the magnetic nozzle rf plasma thrusters including theoretical, numerical, and experimental studies. This type of thrusters are typically called helicon thrusters since the plasma density is enhanced by a helicon wave when applying static magnetic fields to the inductively-coupled rf plasma source operated in the range of MHz. Finally, a recently proposed application of the helicon thruster to the space debris removal, a radiofrequency power system, and permanent magnet configurations for the magnetic nozzle formation are also mentioned.

2 Radiofrequency magnetic nozzle plasma thrusters

To transfer an electric power to the plasma which does not contact any electrodes, one of the rf, microwave, and light powers have to be used to ionize the propellant and/or heat the charged particles. Furthermore, some types of the thrusters utilize the plasma expansion along the magnetic nozzle. The electrodeless magnetic nozzle thruster using an electron cyclotron resonance (ECR) heating were already described in 1968 (Jahn 2006); however, the effect of the magnetic nozzle on the thrust generation has been gradually understood in recent years. Several types of the electrodeless plasma thrusters are sketched in Fig. 2.

A variable specific impulse magnetoplasma rocket (VASIMR) shown in Fig. 2a consists of two sections: a high-density helicon plasma source section and an ion cyclotron resonance heating (ICRH) section (Chang-Diaz 2000). The high-density plasma produced by the helicon source is guided by the strong external magnetic field and the ions are heated by the ICRH section in the direction perpendicular to the magnetic field lines, where the rf frequency for the ICRH has to be equal to the ion cyclotron frequency. The increased perpendicular energy of the ions is converted into the axial flow energy in the magnetic nozzle, based on the conservation laws of the magnetic momentum and kinetic energy of the ions. In this method, most of the rf electric power is coupled with the ions and their thermal energy is utilized to generate the thrust force. To couple the rf power to the ions via the ICRH, very strong magnetic field above 1–2 T is required in VASIMR; hence, superconductor magnets are used. The previous laboratory experiments have shown a thruster efficiency exceeding about 50% when increasing the total rf power up to $\sim$ 200 kW (Longmier et al. 2011, 2014).

Contrary to the VASIMR, the rf or microwave power is efficiently coupled primarily with electrons via Joule- or wave-heating processes in the inductively-coupled plasma (ICP) thrusters (Fig. 2b), the helicon plasma thrusters (Fig. 2c), and the ECR thrusters (Fig. 2d), where the energized electrons collide with neutrals of the propellant gas and the high-density plasma is produced via ionization processes. The detailed

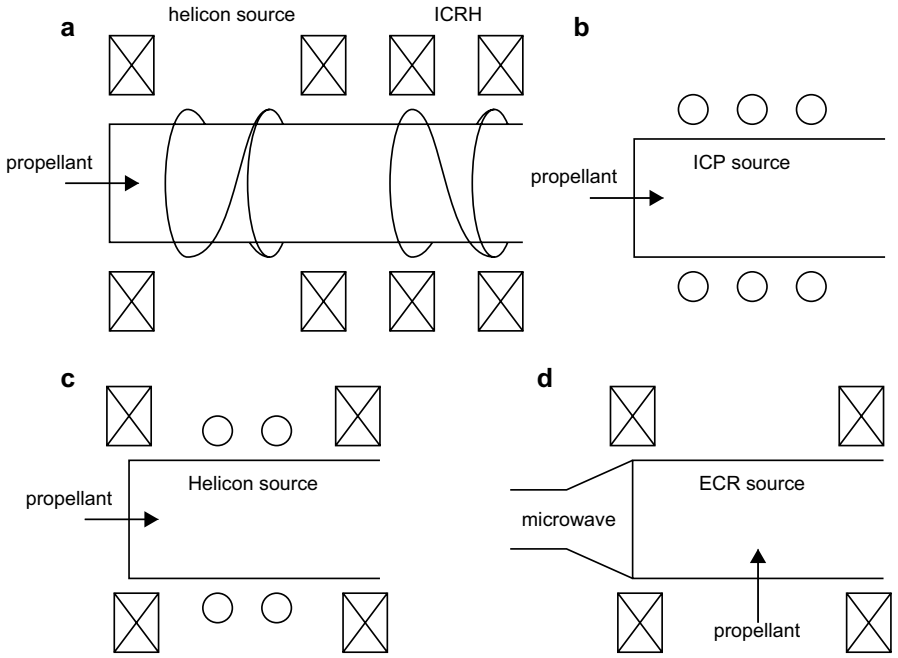

Fig. 2 Schematic diagram of **a** the variable specific impulse magnetoplasma rocket (VASIMR), **b** the inductively-coupled plasma (ICP) thruster, **c** the helicon plasma thruster, and **d** the electron cyclotron resonance (ECR) plasma thruster

heating mechanisms in the inductively-coupled plasmas have been described in many researches and textbook, e.g., in Chap. 11–13 of Lieberman and Lichtenberg (2005). For the helicon and ECR plasma sources, the electric power is once transferred to the wave propagating in the plasmas under static magnetic fields, being called a whistler mode, and the waves efficiently heat the electrons. It is very important to understand the wave characteristics for designing the helicon and ECR thrusters. A number of studies on the helicon sources (not the thrusters) have been performed for the last several decades, e.g., in Listano et al. (1971), Stenzel (1976), Boswell and Chen (1997), Chen and Boswell (1997), Takahashi et al. (2005a, b), Stenzel and Urrutia (2015), Stix (1962) and Swanson (2003).

Very briefly, a dispersion relation (ω–k diagram with the wave angular frequency ω and the wavenumber k) can be derived from Maxwell's equations including a dielectric tensor $\mathbf{K}$ following Swanson's notation (2003). The dielectric tensor is given as

$$\frac{\omega^2}{c^2}\mathbf{K} = \begin{pmatrix} \kappa_1 & \kappa_2 & 0 \\ -\kappa_2 & \kappa_1 & 0 \\ 0 & 0 & \kappa_3 \end{pmatrix}, \tag{3}$$

with κ_1, κ_2, and κ_3 defined by

$$\frac{c^2}{\omega^2}\kappa_1 = 1 - \sum_j \frac{\omega_{pj}^2}{\omega^2 - \omega_{cj}^2},$$
$$i\frac{c^2}{\omega^2}\kappa_2 = \sum_j \frac{\epsilon_j \omega_{cj}\omega_{pj}^2}{\omega(\omega^2 - \omega_{cj}^2)},$$
$$\frac{c^2}{\omega^2}\kappa_3 = 1 - \sum_j \frac{\omega_{pj}^2}{\omega^2},$$

where ω_{pj}, ω_{cj}, and ϵ_j are the plasma frequency, the cyclotron frequency, and the sign of the charge for species j, respectively. The dispersion relation can be written as (Swanson 2003)

$$(\gamma^2 + \kappa_2^2 + \gamma k_\perp^2)\kappa_3 + k_\perp^2[\kappa_1(\gamma + k_\perp^2) - \kappa_2^2] = 0, \tag{4}$$

where $\gamma \equiv k_\parallel^2 - \kappa_1$, $k_\parallel$ and $k_\perp$ are the axial and radial wave numbers, respectively.

Let us consider the most simplified case that the electromagnetic wave propagates along the magnetic field lines, i.e., the perpendicular wavenumber $k_\perp$ is zero. The calculated dispersion for the typical plasma density and the magnetic field strength are shown in Fig. 3, where both the region of the helicon and ECR waves are indicated by dotted ellipses. The three branches can be found in Fig. 3 and labeled as 'R wave' and 'L wave', corresponding to right- and left-hand polarizations,

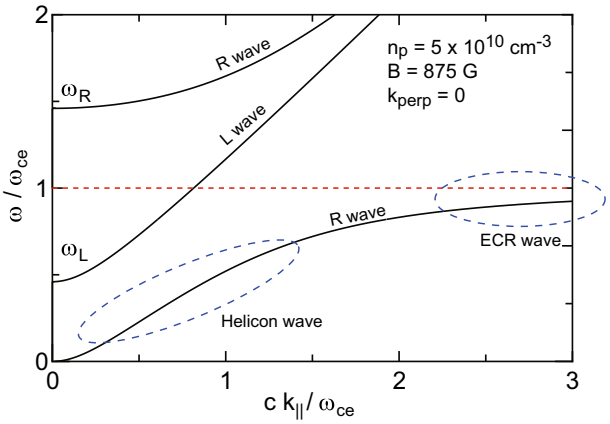

Fig. 3 Dispersion relation (ω–k diagram) of the electromagnetic wave propagating along the magnetic field in plasmas for the typical plasma density of $n_p = 5 \times 10^{10}$ cm^{-3} and magnetic field strength of $B = 875$ G

respectively. The two wave branches have cutoff conditions ($k = 0$) at the specified frequencies given by

$$\omega_{\mathrm{R}} = \frac{\omega_{\mathrm{ce}} + \sqrt{\omega_{\mathrm{ce}}^2 + 4\omega_{\mathrm{pe}}^2}}{2}, \tag{5}$$

$$\omega_{L} = \frac{-\omega_{\mathrm{ce}} + \sqrt{\omega_{\mathrm{ce}}^2 + 4\omega_{\mathrm{pe}}^2}}{2}, \tag{6}$$

as seen in Fig. 3. The helicon and ECR waves are essentially the whistler mode having the right-hand polarization and a resonance condition ($k = \infty$) at $\omega = \omega_{\mathrm{ce}}$. It should be mentioned that the boundary conditions in laboratory plasmas result in the finite parallel and perpendicular wavenumbers and the dispersion relation is modified. Studies on the helicon wave have shown the high-density plasma production in the density range of 10^{12}–10^{13} cm^{-3} under a low gas pressure (typically a few mTorr) (Boswell and Chen 1997; Chen and Boswell 1997; Degeling et al. 1996; Chen and Hershkowitz 1998; Franck et al. 2003; Sakawa et al. 2003; Shinohara et al. 2010). Since the helicon wave has no strict resonance condition as seen in Fig. 3, the helicon source can be operated over a wide range of the magnetic field strength. To heat the electrons by the ECR wave, the wave frequency (ω) has to be equal to the electron cyclotron frequency ω_{ce}; the source has to contain the ECR magnetic field strength in the device, being 875 Gauss for 2.45 GHz microwave. Since the ECR wave has a cutoff region at the lower magnetic field strength ($\omega/\omega_{\mathrm{ce}} > 1$) as seen in Fig. 3, the wave is typically launched from the high magnetic field side so as not to experience the cutoff region. In actual devices, since the plasma sources have both axial and radial boundaries, the analysis of the plasma-filled waveguide mode is required to understand the wave propagation (Takahashi et al. 2005a, b; Swanson 2003). When utilizing these low-pressure discharges for the source, the collisional energy transfer from the electrons to the ions rarely occurs in the range of the density being considered; the plasma is in non-equilibrium, i.e., the thermal energy of the electrons is much larger than that of the ions. Hence it is also important to understand how the electron thermal energy can be converted into the thrust energy, which will be one of the main topics in this review. In a number of experiments, spontaneous ion accelerations due to formations of a current-free double layer (CFDL) and ambipolar electric field are observed in helicon sources as described in Sect. 5.2; application of this ion acceleration phenomenon to the thruster has been proposed, being called a helicon double layer thruster (HDLT) (Charles 2009). When looking at the downstream side of the source having the external magnetic field, the magnetic field diverges and the magnetic nozzle is inevitably formed. It is also a key issue to understand the role of the magnetic nozzle in the electron-energy-dominated thrusters.

3 Diagnostics of plasmas and thrusters

In this section, diagnostics of plasmas and thrusters, which have been used in experiments relating to the helicon thruster and give much insight into the thruster development and underlying the fundamental physics, are very briefly described.

3.1 Plasma diagnostics

As already described in Sect. 1, the physical quantities relating to the thrust imparted by the propulsion devices are the density n, the temperature T, and the velocity v. For plasmas, these physical quantities for both the ions and the electrons have to be considered. It should be mentioned that the temperature is obtained with assuming a Maxwellian energy distribution and the velocity is the macroscopic quantity averaged in the velocity space. These are typically obtained by electrostatic probes in plasmas.

Langmuir probe would be the most popular technique to estimate the density, the electron temperature, and the plasma potential from its I–V characteristic. After estimating the electron temperature with assuming the Maxwellian electron energy distribution, the plasma density n_p consisting of singly charged ions is often obtained from the ion saturation current I_is and the relation of

$$I_\mathrm{is} = 0.61 e n_\mathrm{p} u_\mathrm{B} S, \tag{7}$$

where e, u_B, S are the elementary charge, the Bohm velocity, and the collecting area of the Langmuir probe (Hutchinson 2002). The Bohm velocity is given by $u_\mathrm{B} = \sqrt{k_\mathrm{B} T_\mathrm{e}/m_\mathrm{i}}$ with the Boltzmann constant k_B and the ion mass m_i. However, a sheath formed around the Langmuir probe is extended by the negative bias voltage; the plasma density seems to be often overestimated as described in Chap. 3.2.2 in Hutchinson (2002). Sheridan analyzed the sheath expansion effect on the Langmuir probe diagnosis by a particle-in-cell simulation (Sheridan 2000) and the validity has been shown by an experiment (Lee and Hershkowitz 2007). The velocity v is also estimated by a Mach probe consisting of two probe tips as described in Chap. 3.3.4 of Hutchinson (2002) and Ando et al. (2005) and Chung (2012) or a directional Langmuir probe having a rotational shaft (Nagaoka et al. 2001), however, the calibration coefficient includes uncertainty to obtain the absolute value of the velocity and the velocity obtained here is a macroscopic quantity averaged in the velocity space. Great efforts have been made to obtain the calibration coefficient so far with combining physical consideration (Nagaoka et al. 2001) and the other diagnostics (Terasaka et al. 2010). In rf discharges operated in MHz range, the potential oscillation often distorts the I–V characteristic of the Langmuir probe and significantly affects the estimation of the electron temperature. In that case, an rf-compensated Langmuir probe including the choke coils having a LC resonance at the rf frequency and the reference electrode is a useful method as designed in Sudit and Chen (1994).

In most of the low-pressure discharges, the energy/velocity distributions of the ions and electrons are rarely Maxwellian. The non-Maxwellian distributions are

often induced by a charge-exchange collision between the flowing ions and the neutrals for ions (Charles et al. 1991) and by a non-local effect of the sheath in laboratory plasmas or collisional processes having the cross section nonlinearly depending on the energy for electrons (Kortshagen et al. 1994; Godyak et al. 1995, 2002). Therefore, the detailed measurements of the energy distributions have revealed many aspects of physics in the magnetic nozzle plasmas. The ion energy distribution function (IEDF) can be often obtained by a retarding field energy analyzer (RFEA), consisting of a collector electrode and a few grids including an electron repeller and a discriminator. By sweeping the applied voltage to the discriminator, the energy of the ions flowing into the collector can be selected. Hence the IEDF can be typically obtained by differentiating the collector current–discriminator voltage characteristic. The experiments relating to this review topic have shown both accelerated and thermal ions in the magnetic nozzle, where the spontaneous electrostatic accelerations occur in the magnetic nozzle plasmas (Charles and Boswell 2004; Takahashi et al. 2009) and the signal due to the thermal ions appears around the discriminator voltage equal to the local plasma potential. More precise measurement of the ion velocity distribution function can also be obtained by a laser-induced fluorescence (LIF) method, where the Doppler shift effect on the pumping laser is utilized (Cohen et al. 2003; Biloiu et al. 2005, 2008). By applying the LIF to the magnetic nozzle plasma configuration, spontaneous acceleration of the ions has been observed as described later. The electron energy distribution/probability function (EEDF/EEPF) can be obtained from the second derivative of the *I*–*V* characteristic of the Langmuir probe, which is based on the Druyvesteyn method as described in Chap. 6.6 of Lieberman and Lichtenberg (2005). Since the second derivative is strongly affected by a digital noise in the digitized signal, special techniques have been used for obtaining the second derivative, e.g., an analogue differentiation method (Schoenberg 1978; Takahashi et al. 2010) and an AC superimposition method (Kortshagen and Schlüter 1991; Kang et al. 2017), detecting the signals with resolutions over 2–4 orders of magnitude.

In plasmas, the motion of the charged particles can sometimes generate the internal current and the resultant magnetic field even in current-free plasmas. Measurement of the internal-current-induced magnetic field can give important information to discuss electromagnetic plasma acceleration processes induced by a Lorentz force and plasma-induced modification of the magnetic field structure, e.g., as performed in Tobari et al. (2007) and Roberson et al. (2011). Hence the measurement of the plasma-induced magnetic field is also an important technique to discuss the thrust-generation physics and the plasma dynamics in the magnetic nozzle. The magnetic field induced by the plasma current can be measured by a B-dot probe and a Hall element probe in pulsed and steady-state plasmas, respectively (Stenzel and Urrutia 2000; Corr and Boswell 2007). The internal plasma-induced current density $\mathbf{J}$ can be obtained by taking a rotation of the magnetic field, i.e., $\nabla \times \mathbf{B} = \mu \mathbf{J}$.

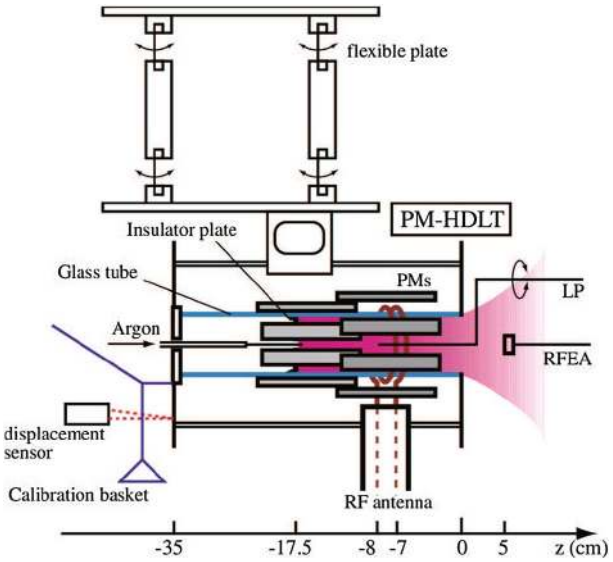

Fig. 4 Schematic diagrams of the thrust stands used for the direct thrust measurement of helicon double layer thrusters (Takahashi et al. 2011a). Figure 4 is taken from Takahashi et al. (2011a)

3.2 Thrust and momentum flux measurement

As described above, great efforts have been made to measure the physical quantities (e.g., density, temperature, velocity, velocity/energy distribution functions, and so on) in low-pressure and low-temperature plasmas over the last several decades. However, the absolute values of the quantities are indeed difficult to be identified and detailed spatial profiles have to be measured to estimate the absolute values of the thrust, i.e., the spatially integrated momentum flux exhausted from the system. Therefore, the thrust force has to be directly measured to assess the thruster performance. Furthermore, the direct thrust measurement and the momentum flux measurement sometimes give useful insight into the plasma dynamics when combining the data from the plasma diagnostics. Here some techniques used in the magnetic nozzle thruster experiments are briefly described.

Two experiments on the direct thrust measurements of the helicon-type plasma thruster have been reported in 2011, where one used solenoids (Pottinger et al. 2011) and the other used permanent magnets (Takahashi et al. 2011a) to provide the magnetic fields. Figure 4 shows the schematic diagrams of the permanent magnet helicon double layer thruster (PM-HDLT) attached to a pendulum thrust balance. The whole structure of the thruster is attached to a pendulum immersed in vacuum for both the experiments; the force exerted to the thruster structure induces displacement of the pendulum. The displacement of the thrust balance can be measured by various methods, such as laser displacement sensors, light-emitting diode displacement sensors, and strain gauges. To obtain the absolute value of the force, a calibration coefficient relating the displacement to the force has to be measured. Various

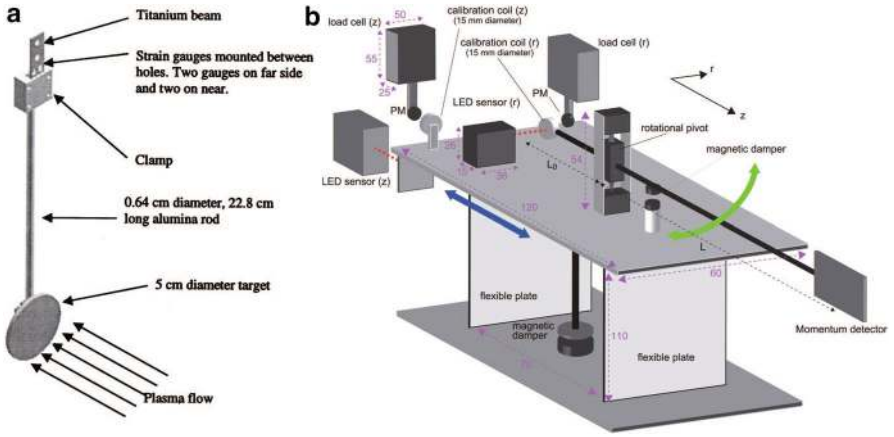

Fig. 5 Schematic diagrams of **a** the momentum flux measuring instrument used in the VASIMR experiments (Chavers and Chang-Diaz 2002) and **b** the momentum vector measurement instrument used in the helicon thruster experiments (Takahashi et al. 2018). **a**, **b** are taken from Chavers and Chang-Diaz (2002) and Takahashi et al. (2018), respectively

types of the thrust balance have been used in assessment of the electric propulsion devices and unique balances providing the thrust vector measurement have also been developed (Nagao et al. 2007; Spethmann et al. 2017).

When it is difficult to attach the thruster structure to the balance for some reasons such as its weight and size, target-type momentum flux measurement instruments have been employed, e.g., Chavers and Chang-Diaz (2002) in the VASIMR experiments and West et al. (2009) and Ling et al. (2010) in the HDLT experiments, where the schematic of the structure is shown in Fig.5a and the displacement of the target is induced when the charged and neutral particles transfer their momentums to the plate. However, one should be careful about overestimation of the thrust force due to sputtering of the target materials and recoil particles at the target surface, which significantly depends on the energy and flux of the incident ions to the target. Therefore, some researches have validated the target measurement by comparing the thrust stand and the target (Longmier et al. 2009; Takahashi et al. 2015), where the measurement of the impulse bit imparted by the pulsed helicon thruster was also demonstrated (Takahashi et al. 2015) for future assessment of the pulsed helicon MPD thruster (Takahashi et al. 2014). When using a small target plate, the target-type balance can yield the local momentum flux, i.e., it could give the spatially resolved measurement of the momentum flux. Furthermore a momentum vector measurement instrument providing the flux of the axial and radial momentums to the target surface has also been developed as shown in Fig. 5b (Takahashi et al. 2018) to further understand the previously observed momentum transfer to the source wall (Takahashi and Ando 2017).

Once again, the plasma diagnostics described here can provide the local physical quantities and the energy distributions of the charged particles, while it often seems to be difficult to identify their absolute values. On the other hand, the thrust and momentum flux diagnostics can provide the absolute values of the force and the momentum

flux. Combination of these diagnostics will provide interesting exploration of the physics underlying the thruster development.

4 Thruster model

In this section, theoretical thruster models are described. As already mentioned, the thrust is equal in magnitude and opposite in direction to the total momentum flux exhausted from the system, which is derived from the momentum conservation law, being equivalent to action-reaction law. Since the total momentum flux T of the fluid having its cross section A is the sum of the static and dynamic pressures integrated over the cross section, it can be generally given as

$$T = \int_A (p_\mathrm{e} + m_\mathrm{i} n_\mathrm{p} u_z^2) \mathrm{d}A, \tag{8}$$

when assuming the cold ions and the negligible electron dynamic pressure (or electron inertia); the momentum flux τ per unit cross section is described as

$$\tau = p_\mathrm{e} + m_\mathrm{i} n_\mathrm{p} u_z^2. \tag{9}$$

It has been proposed that plasma acceleration should occur when the increasing cross section of the flow results from a divergent magnetic field, so that $B(z)A(z) = \mathrm{const}$, $B(z)$ being the intensity of the magnetic field (Manheimer and Fernsler 2001). The external force accelerating the plasma flow in the axial direction seems to be the magnetic pressure force (Hole and Simpson 1997). Sasoh has analyzed the similar thruster model earlier for the MPD thruster (Sasoh 1994). Fruchtman has predicted in one-dimensional model that a spontaneously formed electric field does not impart a momentum to plasmas, while the thrust increases along the axis in the magnetic nozzle (Fruchtman 2006). This model shows the equation similar to the physical nozzle analysis. After that, Ahedo and Merino showed more detailed two-dimensional model assuming the electron streamlines tied to the magnetic field lines, predicting the internal current in the magnetic nozzle (Ahedo and Merino 2010). They concluded that the major force exerted to the magnetic nozzle is coming from an electron Hall current. In these models, the momentum loss at the plasma source wall has not been taken in account; a simple model taking into account the loss of the axial momentum to the radial wall is described here to capture physical pictures of the thrust generation and loss (Takahashi et al. 2011b, 2012).

The axial momentum flux is essentially derived from momentum equations of the ions and electrons. The momentum equation for particle species j in steady-state is given as

$$m_j \nabla (n_j \mathbf{v}_j \mathbf{v}_j) = q_j n_j (\mathbf{E} + \mathbf{v_j} \times \mathbf{B}) - \nabla p_j, \tag{10}$$

where m_j, n_j, $\mathbf{v}_j$, q_j, p_j are the mass, density, velocity, charge, and pressure of the particle species j, respectively. $\mathbf{E}$ and $\mathbf{B}$ are the electric-field and magnetic-field vectors, respectively. $\mathbf{v}_j\mathbf{v}_j$ is the dyadic expression of the velocity vector; $m_j \nabla (n_j \mathbf{v}_j \mathbf{v}_j)$ being equivalent to the inertial term $m_j n_j (\mathbf{v}_j \cdot \nabla)\mathbf{v}_j$ when the continuity equation

$\nabla(n_j \mathbf{v}_j) = 0$ is satisfied. Assuming negligible ion temperature (pressure), negligible electron inertia, and quasi-neutrality ($n_e \sim n_i = n_p$), and considering an axisymmetric system, the radial and axial components of the momentum equations can be written as

$$-en_p(E_r + v_\theta B_z) = \frac{\partial p_e}{\partial r}, \tag{11}$$

$$-en_p(E_z + v_\theta B_r) = \frac{\partial p_e}{\partial z}, \tag{12}$$

$$en_p(E_r + u_\theta B_z) = 0, \tag{13}$$

$$en_p(E_z - u_\theta B_r) = \frac{1}{r}\frac{\partial}{\partial r}(rm_i n_p u_r u_z) + \frac{\partial}{\partial z}(m_i n_p u_z^2), \tag{14}$$

where (v_r, v_θ, v_z), and (u_r, u_θ, u_z) are the velocities of electrons and ions, respectively. It should be mentioned that the radial ion inertial term is neglected for simplicity, while it has been taken into account in the model analyzed by Ahedo and Merino (2010). But the simplified model has been in fair agreement with the laboratory thruster experiment (Takahashi et al. 2011b, 2012).

By eliminating the axial electric field E_z from Eqs. (12) and (14), the momentum flux τ is given as

$$\frac{\partial \tau}{\partial z} = \frac{\partial}{\partial z}(p_e + m_i n_p u_z^2), \tag{15}$$

$$= en_p(v_\theta - u_\theta)B_r - \frac{1}{r}\frac{\partial}{\partial r}(rm_i n_p u_r u_z), \tag{16}$$

where the first term of the right-hand side (RHS) is the Lorentz force arising from the azimuthal net current and the radial magnetic field. Substituting the net current obtained from Eqs. (11) and (13) to Eq. (16) and assuming a source radius r_s and a plasma radius $r_p(z)$ expanding along the magnetic nozzle, the thrust can be derived from Eq. (8) as

$$T = T_s + T_B + T_w, \tag{17}$$

$$T_s = 2\pi \int_{r_s} r p_{e0} \mathrm{d}r, \tag{18}$$

$$T_B = -2\pi \int_z \int_{r_p} r \frac{B_r}{B_z} \frac{\partial p_e}{\partial r} \mathrm{d}r\mathrm{d}z, \tag{19}$$

$$T_w = -2\pi \int_z \int_{r_p} \frac{\partial}{\partial r}(rm_i n_p u_r u_z) \mathrm{d}r\mathrm{d}z, \tag{20}$$

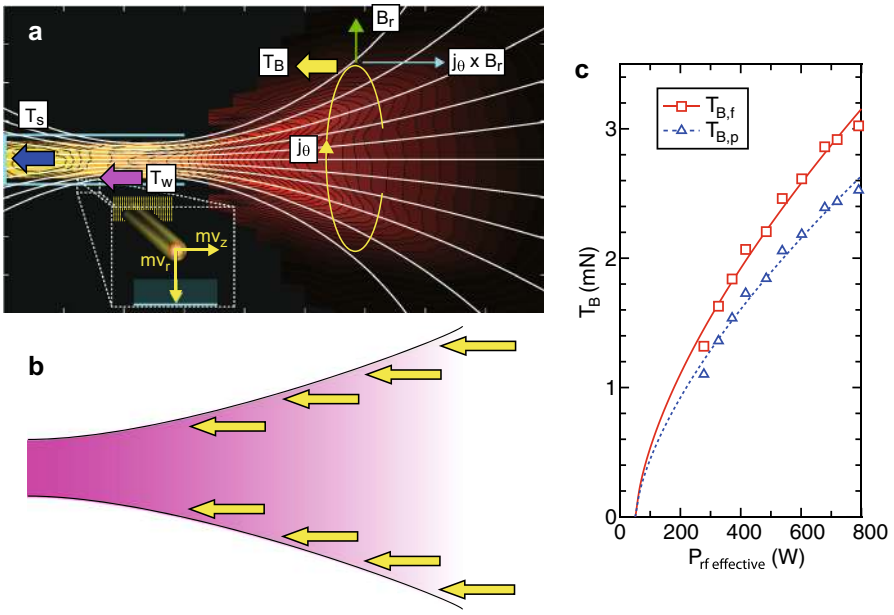

Fig. 6 **a** Physical description of the thrust components in the two-dimensional model. **b** Magnetic nozzle effect in one-dimensional model equivalent to the physical nozzle. **c** Comparison of the thrusts calculated using the two-dimensional [$T_{B,f}$ given by Eq. (19): open squares] and one-dimensional [$T_{B,p}$ given by Eq. (22): open triangles] models, where the experimentally measured plasma parameters for each rf power and the magnetic field configuration are used for the calculation (Fruchtman et al. 2012). Solid and dotted lines are added as visual guides. **c** is taken from Fruchtman et al. (2012)

where p_{e0} is the maximum electron pressure inside the source and T_s corresponds to the constant of the integration. It should be mentioned that the axial ion velocity is assumed to be zero at the maximum pressure position. The physical descriptions of these components are drawn in Fig. 6a and briefly described below.

The T_s term corresponds to the static electron pressure force inside the source pushing the upstream back plate of the thruster source tube, where the electron pressure is converted into the ion dynamic momentum via the sheath acceleration; simultaneously the equal momentum flux flows toward the downstream source exit (Takahashi et al. 2011a; Fruchtman 2006; Lafleur et al. 2011).

The T_B term shows the volume integration of the Lorentz force arising from the radial magnetic field B_r and the azimuthal electron-diamagnetic current $B_z^{-1}\partial p_e/\partial r$, which increases the axial momentum flux of the plasma and the force directing the upstream side is exerted on the magnetic field lines as indicated in Fig. 6a. It should be noted that the electron-diamagnetic drift current can induce the magnetic field opposite in direction to the applied magnetic field. This physical picture of the thrust generation is very similar to the repulsion force when having two permanent magnets which have their N poles face-to-face; then one push the other. Since the source of this term is the radial electron pressure as seen in Eq. (19), the role of the magnetic nozzle for the plasma, in which the electrons are responsible for its energy, is the conversion of the radial electron pressure to the axial plasma momentum via the Lorentz force. When

considering the uniform pressure profile and the discontinuous pressure change at the nozzle surface, the azimuthal current and the Lorentz force is indeed localized at the edge of the plasma column, i.e., at the nozzle surface. This analogy is very similar to that in the physical nozzle as shown in Fig. 6b, where the pressure exerted on the nozzle surface pushes the structure. This was actually proven by re-writing the two-dimensional model into the one-dimensional model (Fruchtman et al. 2012), assuming the expansion of the plasma cross section along the magnetic nozzle ($B_z A = \text{const}$). In the Fruchtman's model, the T_{total} can be written in a manner similar to the physical nozzle as

$$T_{\text{total}} = \int_{A_i}^{A(z)} \langle p_e(z) \rangle \mathrm{d}A', \tag{21}$$

where A_i is the initial cross section of the plasma column and $A(z)$ is the cross section at the axial position z. This term includes both the pressure forces to the source cavity and to the physical nozzle, being equivalent to T_s and T_B, respectively. Using the relation of $B_{z0}A = const$ and assuming the radially uniform magnetic field strength ($B_z(r,z) = B_z(0,z) = B_{z0}$), the T_B term included in Eq. (21) can be written as

$$T_B = -\int_0^z \langle p_e(z) \rangle A(z) \frac{1}{B_{z0}} \frac{\partial B_{z0}}{\partial z}. \tag{22}$$

Figure 6c shows the thrusts calculated by using the two-dimensional ($T_{B,f}$ given by Eq. (19): open squares) and one-dimensional ($T_{B,p}$ given by Eq. (22): open triangles) models, where the experimentally measured plasma parameters for each rf power and the magnetic field configuration are used for the calculation (Fruchtman et al. 2012). The calculation in one-dimensional model shows the discrepancy by 15–25% compared with the two-dimensional calculation for the given magnetic field configuration and the plasma pressure profile (Fruchtman et al. 2012) as shown in Fig. 6c. This discrepancy originates from the approximation of the uniform magnetic field strength along the radial axis. However, this can quickly and roughly give the thrust value once if the axial density profile is measured in the experiment.

The T_w term can be re-written as

$$T_w = -2\pi \int_{r_s} r_s m_i n_w u_{rw} u_{zw} \mathrm{d}z, \tag{23}$$

with the source radius r_s, and the radial and axial velocities (u_{rw}, u_{zw}) of ions at the source wall. Therefore, this term corresponds to the axial momentum ($m_i u_{zw}$) delivered by the ions lost to the radial wall with the flux $n_w u_{rw}$, which have been assumed to be negligible in most of the models (Fruchtman 2006; Ahedo and Merino 2010; Lafleur 2014).

The reaction forces of the above-mentioned force components T_s, T_B, and T_w are exerted to the back wall, the magnetic field lines, and the radial source wall, respectively. Laboratory experiments described later show the direct and individual identification of the three axial force components (Takahashi et al. 2011b, 2013a).

Interesting features have been explored in theoretical studies. Fruchtman has predicted that the ion acceleration induced by spontaneously formed electric fields (such as the CFDL and the ambipolar electric fields) does not impart a momentum to the plasma (Fruchtman 2006). Neglecting the axial momentum flux lost to the radial wall T_w and assuming no magnetic field, the thrust can be given as $T = T_s$ from Eq. (17), being equal to the electron pressure force inside the source. This shows that the electron pressure is converted into the ion dynamic momentum via the electrostatic ion acceleration by the spontaneously formed electric fields. Furthermore, the model predicting neutral depletion effects on the steady-state profile of the plasma density was established, where the plasma and gas are coupled by the neutral depletion and by the wall recombination (Fruchtman 2008a). For the source having the open exit, the axial profile of the plasma density is significantly modified due to the low neutral density near the source exit and the density peak at the upstream side of the source was predicted. These neutral effects were also incorporated in a two-dimensional thruster model (Ahedo and Navarro-Cavallé 2013). Although the charge-exchange collision between the accelerated ions and the neutrals does not change the momentum flux in plasmas, one of the models implies that the momentum gain is increased even if the amplitude of the potential drop is unchanged, when the mean-free path of the charge-exchange collision is smaller than the scale length of the potential drop (Fruchtman 2014). Lafleur has analyzed the energy lost to the axial back wall and the radial wall by a global model; implying that most of the energy is lost to the radial wall by the ions radially accelerated by the radial electric field of the sheath (Lafleur 2014).

It is also important to efficiently couple the electric power with the plasma via rf heating. For the thrusters utilizing the wave-heating phenomena, such as the helicon and ECR thrusters, it is quite important to understand and model the wave propagation in plasmas as in Tian et al. (2018), while the result on the wave analysis has not been compared with the experiments yet as well as the plasma flow models (Ahedo and Merino 2010; Ahedo and Navarro-Cavallé 2013; Merino and Ahedo 2016). The wave propagation is significantly affected by the wall– and plasma–vacuum boundaries; the wave reflection and the resultant standing wave excitation due to an antenna boundary, a rapid change of the magnetic field structure, and a presence of the physical boundaries have been observed in fundamental helicon source experiments (Boswell 1970; Franck et al. 2002; Motomura et al. 2012; Takahashi et al. 2014, 2016). Therefore, analytical models or numerical simulations including the wave propagation in the helicon thruster and comparison with experiments would be useful in near future studies.

5 Laboratory experiments on fundamental physics

In this section, the laboratory experiments ranging from fundamental physics (but relating the magnetic nozzle plasma thruster) to the thrust measurement are described.

5.1 High-density plasma production

The energy source of the thrust generation is essentially only the rf power for the helicon thruster; the design of the plasma source for the high-density plasma production is one of critical issues to improve the thruster performance. Basic laboratory experiments on the helicon source have been conducted with various magnetic field strengths, gas pressures, rf powers, rf frequencies, and plasma cavity sizes. When increasing the rf power, a mode jump to the high-density mode has been observed in a number of experiments and was connected with the helicon wave propagation and the rf power coupling. If the antenna is well-designed so as to yield an efficient power coupling with the plasma in the ICP mode, the density jump may not be clearly observed. However, the presence of the helicon wave often helps the improvement of the power coupling. The density jumps by the helicon wave in the basic laboratory experiments were observed for the case both with the strong (~kG) (Franck et al. 2003; Sakawa et al. 1998) and weak magnetic fields (a few tens of G) (Degeling et al. 1996; Chen 2003; Sato et al. 2004), where the plasma column is typically terminated by the axial boundaries of the experimental devices. Some thruster experiments have observed the transition to the high-density mode under a low magnetic field (Ling et al. 2010; Harle et al. 2013), where both the thrust measurements using the thrust stand and the target stand have shown an increase in the thrust when having a high plasma density for a magnetic field of about 50–100

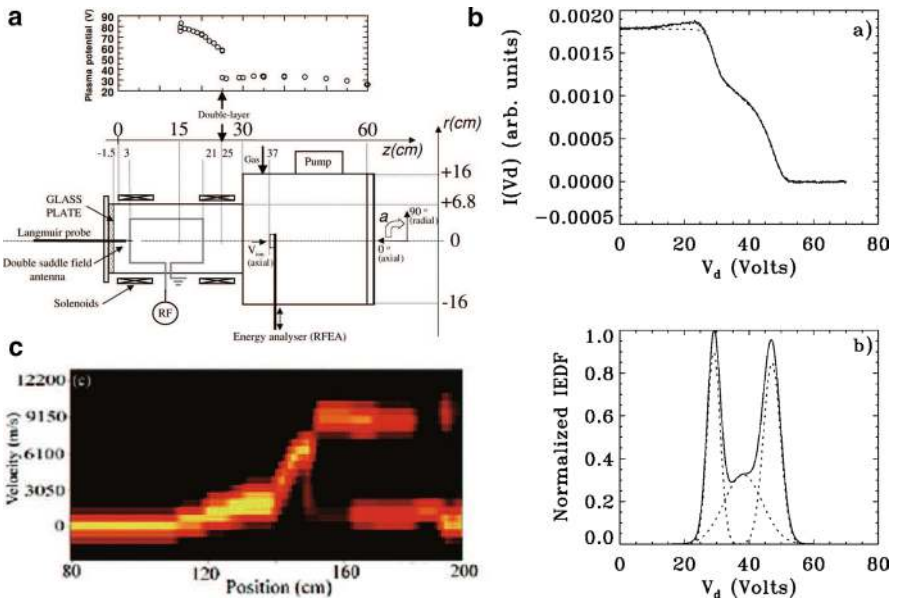

Fig. 7 **a** Schematic of typical setup of a helicon source attached to a diffusion chamber and the measured plasma potential along the axis in Chi-Kung reactor. **b** The *I–V* characteristic of the RFEA and the normalized IEDF downstream of the magnetically expanding helicon source. **c** The ion velocity distribution function measured along the axis in HELIX device. **a** and **b** are from Charles and Boswell (2004) and **c** is from Sun et al. (2005)

G. On the other hand, the transition to the high-density mode has not been clearly observed for the strong magnetic field (or has not been investigated) in the thruster experiments. The difference between the thruster and the basic laboratory experiment is expected to be the presence of the axial boundary downstream of the source. Since both the axial and radial boundaries significantly affect the wave propagations and the wave–plasma interaction, the wave propagation in and the thruster design of the magnetic nozzle thruster for the high-density plasma production are still challenging experimental issues as well as the analytical and numerical studies as briefly mentioned in Sect. 4.

5.2 Ion acceleration by electric fields

A helicon source attached to a diffusion chamber and not immersed in vacuum as shown in Fig. 7a is easier to be operated on than that immersed in vacuum, since the antenna immersed in vacuum frequently induces anomalous and parasitic discharges due to the capacitive coupling and the high-voltage breakdown at the antenna. This type of experiments has clarified and discovered many aspects of physics in the magnetic nozzle. Measurements of the plasma potential (Fig. 7a) and the IEDF downstream of the source using the RFEA (Fig. 7b) and LIF techniques (Fig. 7c) have shown the presence of the two components of the ions consisting of the supersonic beam and the thermal ones in low-pressure operations (Cohen et al. 2003, 2006; Charles and Boswell 2003; Sutherland et al. 2005; Sun et al. 2005; Takahashi and Fujiwara 2011; Wiebold et al. 2011). Charles and Boswell identified that the energy of the supersonic ion beam corresponds to the rapid potential drop with a thickness of about a few tens-hundreds of Debye length (Charles and Boswell 2004). This structure is observed to be sustained in steady state and called the current-free double layer (CFDL). The similar acceleration by ambipolar electric fields having a gradual potential decrease has also been observed in experiments (Charles et al. 1991; Takahashi et al. 2009; Volynets et al. 2006; Corr et al. 2008; Longmier et al. 2011). The accelerated ion flow has also been observed downstream of a high-power helicon source (Prager et al. 2008). Two-dimensional nature of the ion dynamics relating to such electrostatic ion acceleration in the magnetically and/or geometrically expanding plasmas have been investigated in a number of laboratory experiments. The radial measurement of the ion beam has revealed the generation of the collimated supersonic ion beam accelerated by the CFDL (Charles 2005; Cox et al. 2008; Takahashi et al. 2011), where the result in Takahashi et al. (2011) has shown the slight expansion of the ion beam radius along the magnetic field lines near the thruster exit and the deviation downstream of the magnetic nozzle. When changing the gas pressure or gas species, the two-dimensional structure of the potential drop changes from plane to hemispherical structures; then the divergence of the ion beam is simultaneously changed (Takahashi and Fujiwara 2009; Takahashi et al. 2010). Charles et al. have observed a U-shape CFDL having a equipotential surface oblique to the magnetic field lines (Charles et al. 2009). Parametric studies in the laboratories have revealed some features of the CFDLs in the magnetically expanding plasmas. Lieberman and Charles have identified the pressure ranges

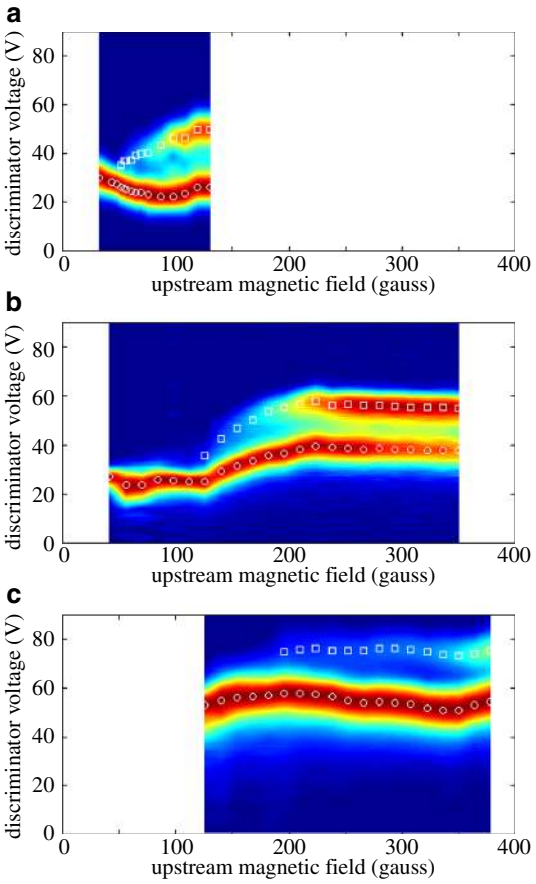

Fig. 8 Normalized IEDFs (contour color) measured in **a** Chi-Kung reactor with a 13.7-cm-diameter source, and in EMPI reactor with **b** a 6.5-cm-diameter and **c** with a 4.6-cm-diameter source tubes, together with the local plasma potential (open circles) and the beam potential (open squares) measured downstream of the sources. Figure is taken from Takahashi et al. (2010)

of the CFDL appearance (Lieberman and Charles 2006). This type of the structure is also observed for various propellant gases, e.g., Ar, Xe, N_2, N_2O, CH_4, CO_2,and so on (Charles et al. 2008). After the magnetic field range for the CFDL formation was experimentally observed (Charles and Boswell 2007), Takahashi et al. have performed the ion-beam measurement when changing the magnetic field and the source diameter. Contour color plots in Fig. 8 show the IEDFs normalized by the maximum value as functions of the magnetic field strength for three different diameter source tubes. The measurements were performed downstream of the source tube; the local plasma potentials downstream of the source are plotted by open circles. The IEDF contains the single peak around the local plasma potential, corresponding to the thermal ions, for the weak magnetic field strengths. When increasing the magnetic field strength, the additional peak at higher potential side appears for all the three cases and implying the formation of the CFDL, where the discriminator voltage giving the second peak is defined as beam potential and plotted by open squares in Fig. 8. It was clearly observed that the threshold of the magnetic field providing the CFDL formation and the ion-beam generation is changed by the source tube

diameter, showing that the CFDL ion acceleration is triggered when the ion Larmor radius calculated with the ion thermal velocity becomes smaller than the source tube radius (Takahashi et al. 2010).

Theory including backstreaming 'beam' electrons generated in and accelerated from the low-potential side has been established and compared with the experiments, showing a good agreement with the DL formation for various gas pressures (Lieberman and Charles 2006). It should be mentioned that the backstreaming 'beam' electrons should be detected as a positive slope in an electron energy distribution at the high-potential side, if they are born in the low-potential side. The physical description of the DL with the beam electrons accelerated from the low-potential to high-potential sides can be found in Hershkowitz (1985). Another model proposed that the DL is actually similar to the sheath formation, showing that the potential drop of the DL is obtained from the current-free condition assuming the Maxwellian electron energy distribution (Chen 2006). The other model has assumed the presence of the high-temperature component of the tail electrons (Ahedo and Sánchez 2009). Meige et al. have shown both the CFDL formation and the ion acceleration in a one-dimensional particle-in-cell (PIC) simulation, where plasma loss term is artificially included downstream of the source (Meige et al. 2005). Then the rapid potential drop following the Boltzmann relation has successfully reproduced in their simulation. Rao and Singh have performed a two-dimensional PIC simulation showing the spontaneous formation of the CFDL (Rao and Singh 2012).

5.3 Electron dynamics

In the above-mentioned DL models, the electron energy distribution in the high-potential side is assumed to contain the backstreaming 'beam' electrons generated in the low-potential side and accelerated by the potential drop (Lieberman and Charles 2006) or the high-temperature tail component (Ahedo and Sánchez 2009), while the 1D-PIC simulation has shown the absence of such energetic electrons in the high-potential side rather than the presence of the high-energy component (Meige and Boswell 2006). The high-density plasma sustained in the high-potential side is also interpreted to be due to the ionization induced by the backstreaming 'beam' electrons (Thakur et al. 2009). Furthermore an instability coexisting with the DL is interpreted as an ionization instability induced by the backstreaming 'beam' electrons (Aanesland et al. 2006). When the electrons are born due to the ionization in the high-potential side, the electrons having an energy less than the potential drop are trapped in the high-potential side, while the high-energy ones can overcome the potential drop of the CFDL and some of them are reflected by the grounded wall sheath and come back to the high-potential side. If they are newly born in the low-potential side via the ionization process, they are electrostatically accelerated from the low- to high-potential sides and should be detected as an electron beam component in the high-potential side, being seen as a positive slope in the upstream EEPF.

The measurement of the electron energy probability function (EEPF) has been firstly performed in 2007 by combination of the rf-compensated Langmuir probe and an analog differentiation technique (Takahashi et al. 2007), showing

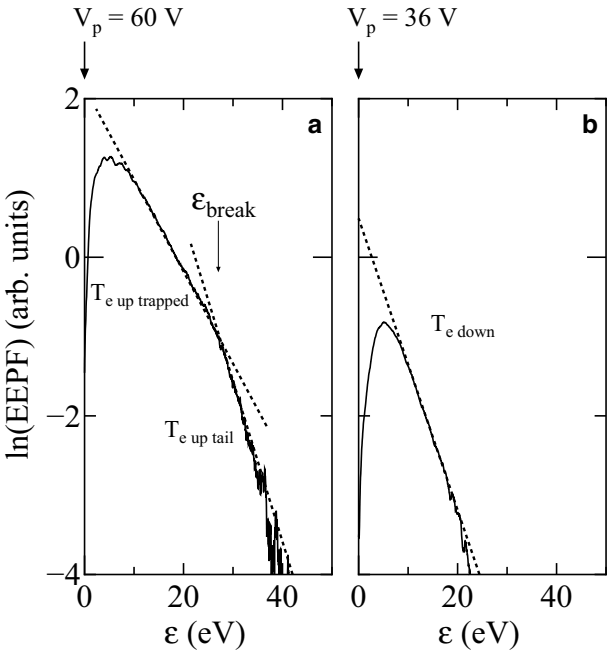

Fig. 9 Natural logarithm plot of the electron energy probability functions (EEPFs) measured in **a** the upstream and **b** downstream area of the CFDL in Chi-Kung reactor. The dashed lines show the tangential lines giving each temperature $T_{\text{e trapped}} \sim 8$ eV, $T_{\text{e up tail}} \sim 5$ eV, and $T_{\text{e down}} \sim 5$ eV. The break energy $\varepsilon_{\text{break}}$ of the EEPF depletion at 27 eV is shown by the arrow in **a**. Figure is taken from Takahashi et al. (2007)

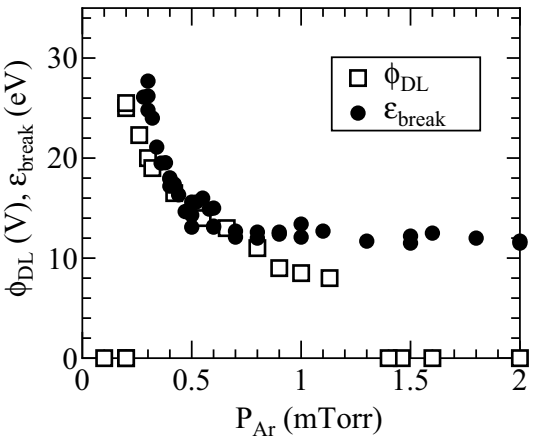

Fig. 10 The break energy $\varepsilon_{\text{break}}$ (filled circles) and the potential drop ϕ_{DL} of the DL (open squares) as a function of the working gas pressure P_{Ar}. Figure is taken from Takahashi et al. (2007)

the depleted tail of the EEPF rather than the 'beam' electrons (Fig. 9a), which is very similar to the 1D-PIC result. Furthermore, the slope of the EEPF measured downstream of the CFDL (Fig. 9b) coincides that of the tail in the upstream EEPF. The break energy $\varepsilon_{\text{break}}$ of the depleted tail is compared with the potential

drop ϕ_{DL} of the CFDL as shown in Fig. 10; they agree well for the low-pressure condition containing the CFDL, while the break energy is close to the argon excitation energy for the high-pressure condition containing no CFDL. These results imply that the CFDL is sustained only by a single source of the plasma located at the high-potential side, where the depleted tail electrons can overcome the potential drop of the DL and give their energy to the potential structure when they are decelerated. These results have proposed that the helicon thruster does not require the neutralizer since the exhausted fluxes of the ions and the electrons are spontaneously balanced, satisfying the zero global net current. In the laboratory system containing the vacuum chamber boundary, the upstream tail electrons overcoming the potential drop of the DL are trapped by the sheath and come back to the source side via the acceleration by the DL. The detailed axial measurement of the EEPFs has shown such a behavior of the electrons, while the low-energy part is confined by the electrostatic potential structure (Boswell et al. 2015). In such a situation, the potential structure affects the shape of the EEPF (called a non-local effect). Similar EEPF has also been detected by Plihon et al. in their DL experiment (Plihon et al. 2017).

Two-dimensional measurements of the EEPFs (Takahashi et al. 2008, 2009) have also related to structural formations in the magnetically expanding plasmas, such as a donut (Cox et al. 2008) and conical density profiles (Charles 2010) near the outer magnetic field lines intersecting the wall at the open source exit. The setup of the

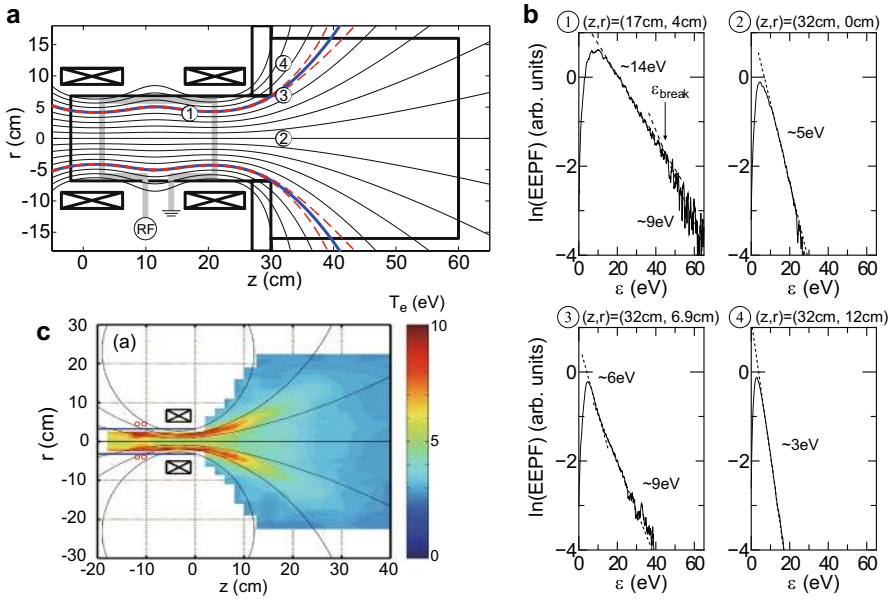

Fig. 11 **a** Schematic diagram of the EEPF measurements in Chi-Kung reactor. **b** The EEPFs measured at the positions labeled as 1–4 in **a**. **c** Two-dimensional profile of the electron temperature measured in the helicon thruster 'HPT-I' immersed in vacuum. Descriptions of 'upstream' and 'downstream' in the main text correspond to the left and right sides of the helicon source in the figures. Figures **a**–**c** are from Takahashi et al. (2009, 2017), respectively

Chi-Kung reactor is shown in Fig. 11a and the representative EEPFs observed at the locations labeled as 1–4 in Fig. 11a are shown in Fig. 11b. The radial measurement of the EEPFs inside the source has shown the significantly high-temperature population consisting of a $\sim$ 14 eV slope for the low-energy part and the depleted tail above $\sim$ 40 eV resulting in a $\sim$ 9 eV slope (Takahashi et al. 2008). This EEPF was observed at the radial location between the outer magnetic field line and the source wall. The most of the 14 eV population electrons are trapped inside the source by the magnetic field lines terminated by the radial source wall. Very close to the outer magnetic field lines intersecting the wall at the source exit, the high-energy electrons having the 9 eV population can be leaked and transported along the magnetic field lines and overcoming the potential drop (Takahashi et al. 2009) as observed at the location 3 in Fig. 11a, b. This leakage of the high-energy electrons and/or the conical density profiles were observed regardless of the absence of the DL (Igarashi et al. 2011; Saha et al. 2014). The high-density conical structure downstream of the source is interpreted as the result of the local ionization by the energetic electrons (Takahashi et al. 2009; Charles 2010). The effect of the ∇B drift resulting in the azimuthal electron rotation has also been discussed (Ghosh et al. 2017). When changing the rf antenna location while maintaining the magnetic field configuration, the radial location of the energetic electrons is changed in the experiment, confirming the generation of the high-temperature electrons by the rf heating and the simple leakage along the magnetic field lines (Takahashi et al. 2017), where the conical structure is also observed downstream of the helicon thruster 'HPT-I' immersed in vacuum as shown in Fig. 11c.

As mentioned at the last paragraph of Sect. 5.2 and the first paragraph of Sect. 5.3, the backstreaming 'beam' electrons generated in and accelerated from the low-potential side, which have to be detected as 'beam' component in the EEPF at the high-potential side, have been thought to sustain the high-temperature or high-density plasmas in the high-potential side and to model the CFDL formation, where the electron temperature estimated from a particle balance equation in a global model assuming a Maxwellian EEPF is significantly lower than the measurement. As analyzed in Takahashi et al. (2011), the EEPF upstream of the CFDL is close to a Druyvesteyn EEPF due to the depleted tail, rather than the Maxwellian EEPF. The shape of the EEPF can be taken into account to the particle balance equation as performed by Gudmundsson (2001); the analysis assuming the Thomson ionization cross section model and the generalized Bohm velocity (Amemiya 1997) was performed in Takahashi et al. (2011). The calculated results by Takahashi et al. are in good agreement with the measurements in two different experimental devices (Takahashi et al. 2011). Therefore, the measured high-electron temperature upstream of the CFDL satisfies the balance between the ionization and loss even if not taking into account the backstreaming 'beam' electrons. This implies that the CFDLs in the magnetically expanding plasmas are a new class of the DLs with no electron beam component generated in and accelerated from the low-potential side. More kinetic model for the formation of the CFDL will be required to fully understand it.

5.4 Electrostatic ion acceleration energy

The potential drop obtained in the CFDL theory has well-described the measured potential drop (Lieberman and Charles 2006), while the upstream 'beam' electrons have to be incorporated to reproduce the CFDL in this model, which is inconsistent with the experiments. According to the researches on the ion and electron dynamics relating to the spontaneous electric field formation, the fluxes of the ions accelerated by and the electrons overcoming the potential drop are balanced so as to maintain the charge neutrality downstream of the CFDL and the zero global current. This dynamics is very similar to that in the sheath at the floating wall and discussed by Chen in early stage of the researches (Chen 2006). The potential drop ΔV for the Maxwellian EEPF is derived from the balance as

$$\Delta V = \frac{1}{2}\left[1 + \ln\left(\frac{m_\mathrm{i}}{2\pi m_\mathrm{e}}\right)\right]\frac{k_\mathrm{B}T_\mathrm{e}}{e} \sim 5.18\frac{k_\mathrm{B}T_\mathrm{e}}{e} \text{ in argon.} \tag{24}$$

This analogy fairly fits the experimental observation showing the 20–30 eV ion beam for the downstream electron temperature of about 5 eV (Charles 2007). In the CFDL experiment, the energy source of the potential drop is that of the electrons overcoming the potential drop, where their energy is transferred via their deceleration by the potential drop. The populations of the tail electrons in the upstream EEPF and the thermal electrons in the downstream EEPF, i.e., the free electrons having sufficient energy overcoming the CFDL, are about 5 eV, and the potential drop observed by Charles and Boswell was about 25 eV. A very high-energy ion beam of 100–200 eV has been observed in the ECR thruster (Cannat et al. 2015), where the measured electron temperature is extremely high and close to 20 eV in the ECR thruster, their high-energy ion beam seems to be consistent with this analogy. However, it should be mentioned that the observed ion-beam energy in the ECR thruster is higher than that expected from Eq. (24); the detailed measurement of the EEPF would be useful to fully understand it, since the Maxwellian EEPF is assumed in Eq. (24) and the value of the ΔV would be changed by the shape of the EEPF. For example, it is modified as $\Delta V \sim 4k_\mathrm{B}T_\mathrm{eff}/e$ with the effective electron temperature T_eff for the Druyvesteyn EEPF (Lieberman and Lichtenberg 2005). As easily expected, the high-energy tail electrons significantly affect the potential drop; the measurement of the EEPF is required to model the potential drop causing the ion acceleration.

5.5 Experiment on thrust-generation mechanisms

To directly measure the thrust, which is the force exerted to the thruster structure, the whole thruster structure has to be attached to the pendulum thrust balance immersed in vacuum. Operating the thruster in vacuum has been performed in some groups. The direct thrust measurement of the force was attempted in Batishchev (2009), where only the plasma source tube is attached to the balance; hence the total thrust force was not assessed. The HDLT was first operated in a large-volume

space-simulation chamber (Charles et al. 2008). West et al. and Ling et al. have applied the target-type momentum flux measurement instrument in a space simulation chamber (West et al. 2009; Ling et al. 2010); the total thrust could not be identified due to the smaller diameter of the target than that of the plasma. Kuwahara et al. used the target-type pendulum larger than the plasma radius to identify the thrust (Kuwahara et al. 2017), where the helicon source rather than the thruster is attached to a diffusion chamber and a strong background magnetic field above 1 kG was applied, which significantly affects the plasma loss via the cross-field diffusion, resulting in overestimating the thrust. Furthermore, the effects of the axial boundary condition on the plasma production, which often induces the density enhancement by a standing wave (Boswell 1970; Motomura et al. 2012; Takahashi et al. 2014, 2016) and by an increase in the local neutral density (called the Clausing factor in Goebel and Katz 2008), were not verified in Kuwahara et al. (2017). Winglee et al. have immersed the very high-power plasma source in the vacuum chamber and successfully operated it with the rf power above 20 kW (Ziemba et al. 2006), while their experiment does not contain the thrust balance. The gas pressure inside the chamber is determined by the balance between the gas flow rate and the pumping speed. Some research groups have used large vacuum facilities having a huge pumping speed; the parasitic discharges are expected to be suppressed when the chamber pressure is maintained low even if the propellant gas is introduced. However, such a huge vacuum facility is indeed difficult to do experiments efficiently for scientific researches. Therefore anomalous discharges, micro arcing, and parasitic discharges, have frequently occurred in some experiments when immersing the source in the vacuum, limiting the source operational conditions (Ling et al. 2011). The rf technique to inhibit the arcing by inserting a blocking capacitor (West et al. 2010) and the parasitic discharges by shielding the antenna (Takahashi 2012) have been successfully tested and significantly contributed to the helicon thruster researches in vacuum.

Although much effort is required to operate the source in the vacuum, such experiments performed by several research groups have discovered many aspect of physics, since the direct measurement of the thrust is equivalent to identification of the fundamental physical quantity of the momentum flux. These are reviewed in this section.

5.5.1 Static pressure force in the source

The direct measurements of the thrust are performed by two research groups at almost the same time in 2011 (Pottinger et al. 2011; Takahashi et al. 2011a), where the magnetic nozzles are applied by two solenoids and the permanent magnets, respectively, and the thruster seems to contain the CFDL and the resultant density drop near the source exit. In these experiments, the thrust of about a few mN was obtained for several hundreds of W. This is very close to the maximum electron pressure inside the source; most of the thrust force seems to originate from the T_s term given by Eq. (18). This is also confirmed by the experiment using an inductively-coupled plasma thruster containing an ambipolar electric field and no magnetic fields (Lafleur et al. 2011). Hence it can be deduced that the spontaneously

formed ambipolar and CFDL's electric fields do not impart significant momentum to the plasma flow as predicted by Fruchtman (2006), since no external momentum is given to the plasma. The role of the spontaneous electric fields is the conversion of the electron pressure to the ion dynamic momentum via the electrostatic acceleration, which is consistent with the electron dynamics described in Sect. 5.3.

5.5.2 Lorentz force in the magnetic nozzle

As described in Sect. 4, the magnetic nozzle might be able to increase the thrust, where the Lorentz force arising from the radial magnetic field and the azimuthal electron-diamagnetic drift current can impart the axial momentum to the plasma. As the origin of the electron-diamagnetic drift current is the radial pressure gradient of the electrons, the role of the magnetic nozzle is the momentum conversion from the radial electron pressure to the axial momentum. Under this situation, the reaction force is exerted to the magnetic field lines, which are generated by the solenoids and/or the permanent magnets. Therefore the measurement of the force exerted to the solenoids and the permanent magnets can identify only the T_B term. The individual measurement of the T_B term has been firstly performed by attaching only the solenoids to the pendulum thrust balance (Takahashi et al. 2011b), whereby the geometrical and magnetic configurations are unchanged as the displacement of the solenoid is only about 10 μm. The source having the solenoids was operated in two different modes; one containing the DL ('A-mode') and the other containing no DL ('B-mode'). Furthermore, the direct measurement of T_{total} imparted by the PM helicon thruster ('C-mode') was also performed. The measured force components T_{total} and T_B are plotted by open squares and circles, respectively, in Fig. 12a–c for the three modes. These results show about one-half of the total thrust is arising from the T_B term for the B-mode case containing no DL, where the density in the magnetic

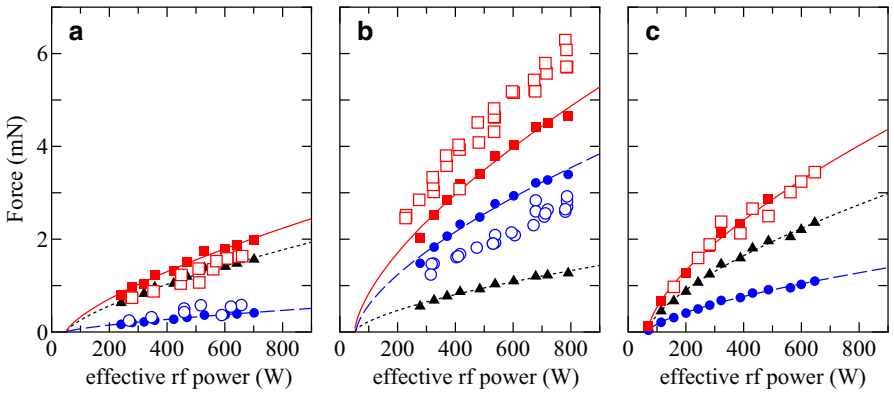

Fig. 12 Directly measured forces T_{total} (open squares) and T_B (open circles) as functions of the effective rf power for the **a** 'A' mode containing a CFDL, **b** 'B' mode containing no CFDL, and **c** 'C' mode having a magnetic nozzle formed by the PMs, respectively. The force components T_s (filled triangles), T_B (filled circles), and T_{total} (filled squares) calculated from Eqs. (18) and (19) are plotted together with the fitted curves added as visual guides. Figure is taken from Takahashi et al. (2011b)

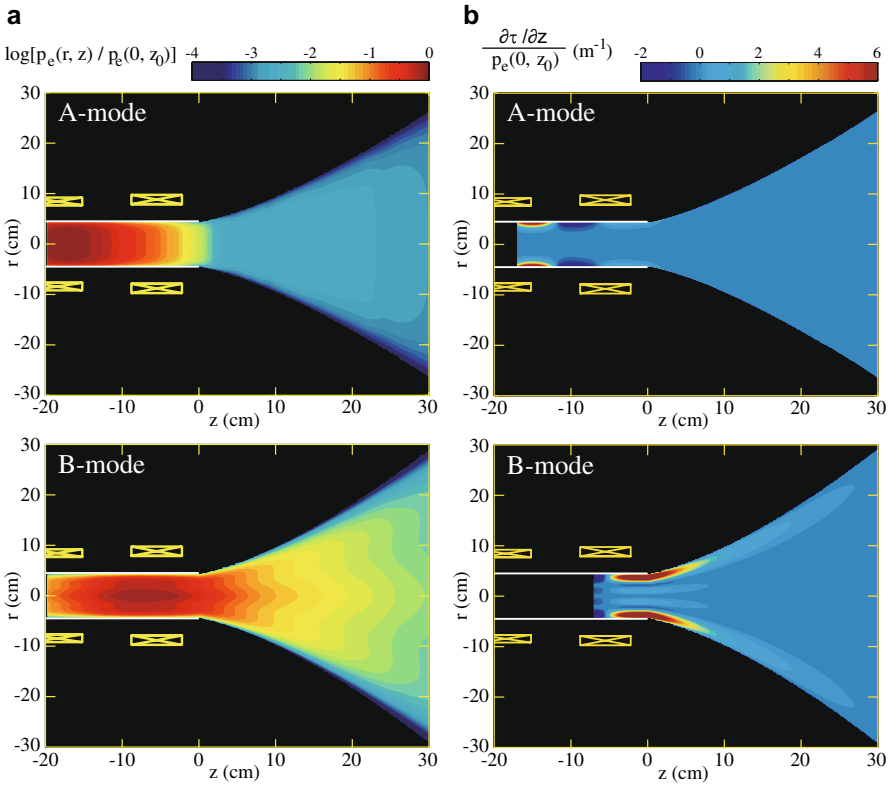

Fig. 13 Two-dimensional profiles of **a** the logarithm of the normalized electron pressure and **b** the force gain per unit cross section $\partial\tau/\partial z$ normalized by the maximum electron pressure $p_e(0, z_0)$. Figure is taken from Takahashi et al. (2012)

nozzle for this case is higher by one order of magnitude than that for the DL case. The two-dimensional profile of the electron pressure is simply modeled based on the radial and axial measurements using the Langmuir probe as shown in Fig. 13a, giving the two-dimensional profile of the gain of the axial momentum flux $\partial\tau/\partial z$ [see Eq. (9)] as shown in Fig. 13b. The T_s and T_B terms were calculated using Eqs. (18) and (19), being the surface and volume integrations of Fig. 13a, b, respectively, where the T_w term is assumed to be negligible. The calculated T_B and T_s forces and the total thrust force T_{total} are in fair agreement (discrepancy within 20–30%) with the directly measured ones as seen in Fig. 12a–c, implying the validity of the theoretical model described in Sect. 4. The two-dimensional profile of $\partial\tau/\partial z$ in Fig. 13b implies that the force is generated near the magnetic nozzle surface where the radial density gradient exists. The similar experiment is also performed with a conical helicon plasma thruster; the pressure force exerted on the conical inner surface has been analyzed and compared with the directly measured force components (Charles et al. 2012).

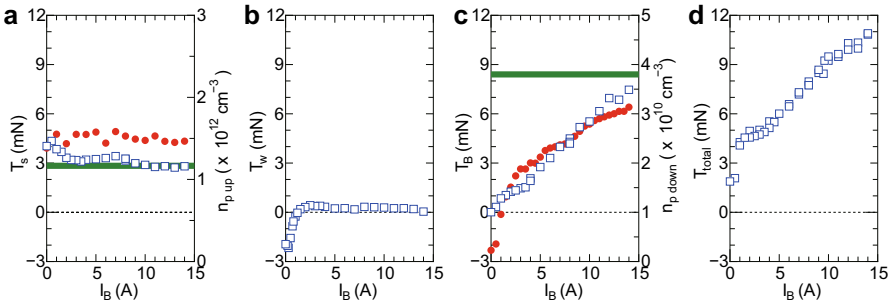

Fig. 14 Individually measured thrust components **a** T_s, **b** T_w, **c** T_B, and **d** the total thrust T_{total} as functions of the solenoid current I_B, corresponding to the magnetic field strength in 'HPT-I'. The filled circles in **a** and **c** show the measured upstream and downstream plasma density, respectively. The bold solid lines in **a** and **c** shows T_s calculated by Eq. (18) and T_B calculated by Eq. (22) assuming no plasma loss from the magnetic nozzle, i.e., the ideal magnetic nozzle approximation, respectively. Figure is taken from Takahashi et al. (2013a)

The individual measurement of the force components was performed in more detail by disassembling the source back wall and radial wall, i.e., the individual measurement of T_s, T_B, and T_w was carried out (Takahashi et al. 2013a). By applying a rapidly convergent–divergent magnetic nozzle near the thruster exit, the magnetic field strength at the rf antenna location is maintained less than 200 Gauss, where the ion Larmor radius is larger than the source tube radius and the plasma loss to the wall is expected to be mostly unchanged. This configuration allowed maintaining the constant source plasma density when changing the solenoid current, while the cross-field diffusion and the plasma density in the magnetic nozzle are successfully inhibited and increased, respectively, when increasing the magnetic field strength. All the components measured individually are plotted by open squares in Fig. 14. The T_s corresponding to the maximum electron pressure inside the source is confirmed to be unchanged because of the constant plasma density inside the source; fairly agreeing with the value calculated from the pressure measurement (bold solid line in Fig. 14a). The T_w term was negligible in this experiment. The T_B term is clearly observed to increase with the increase in the magnetic field strength, which was confirmed to correlate with the density inside the magnetic nozzle (filled circles in Fig. 14c). It can be imagined that the plasma loss from the magnetic nozzle due to the cross-field diffusion can be inhibited when increasing the magnetic field strength to infinity. When assuming no plasma loss from the nozzle and isothermal expansion, the upper theoretical limit of the electron–diamagnetic thrust for a given plasma injection into the magnetic nozzle can be calculated from Eq. (22) as plotted by the bold line in Fig. 14c. It is found that the measured thrust is approaching the theoretical limit; simultaneously the directly measured total thrust T_{total} increases and hence the contribution of the magnetic nozzle effect on the thruster performance is indeed significant.

In the experiment approaching the theoretical limit of the electron-diamagnetic thrust, the detected thrust continues to increase with the increase in the magnetic field in the range of the experiment as seen in Fig. 14c. To verify the

saturation of the thrust for the very strong magnetic field for a given rf power, the solenoid current pulsed by an insulator gate bipolar transistor (IGBT) is applied to the helicon source (Takahashi et al. 2013), where the field strength is successfully increased up to 6 kG with a pulse length of a few tens of ms with the source attached to the diffusion chamber. The increase in the plasma density in the magnetic nozzle and the after saturation is clearly demonstrated by the pulsed magnetic field technique. It seemed to be difficult to use the thrust balance under the pulsed strong magnetic field since a Lorentz force between the magnetic field and the resultant eddy current induced a significant displacement of the thrust balance, which is larger than that induced by the plasma flow. Therefore, the thrust assessment using a target plate having a larger diameter than the plasma diameter was performed. The validity of the target technique was verified by comparing the results with the thrust stand and the target balance with the steady-state force measurements, where the thrusts measured by the two different techniques are in excellent agreement (Takahashi et al. 2015). Furthermore, an impulse bit has to be measured for the pulsed operation of the helicon thruster with the known pulse width; a method to measure the impulse bit was demonstrated prior to the experiment with the strong magnetic field. This technique was applied to the pulsed helicon thruster with the pulsed strong magnetic field immersed in vacuum chamber (Takahashi et al. 2016); the result clearly shows the saturation of the thrust when increasing the magnetic field strength and showed that the inhibition of the cross-field diffusion is a key issue to improve the performance in the future, where the cross-field diffusion processes sometimes originate from the collisional process and the plasma instabilities. Singh et al. have shown the presence of the plasma instability near the surface of the magnetic nozzle in their PIC simulation (Singh et al. 2013). The experimental investigations on the plasma instabilities and the resultant particle transport have not been performed yet in detail and remains further experimental issue.

The T_{B} term given by Eq. (19) is indeed simplified model neglecting the radial ion inertia term. Furthermore, the electron Hall current is canceled by the ion $\mathbf{E} \times \mathbf{B}$ drift in the model, which would be valid for the magnetized ions. However, the ions are easily unmagnetized when the magnetic field strength decreases along the axis in the magnetic nozzle, while more detailed magnetic nozzle effect including the radial ion inertia term has been computed by Ahedo and Merino previously (Ahedo and Merino 2010). Since the T_{B} term is the Lorentz force due to the radial magnetic field and the azimuthal plasma-induced current, the measurement of the plasma-induced current can indirectly give the local Lorentz force exerted on the plasma flow and also on the magnetic field lines. This technique has been performed previously for identifying the plasma acceleration processes in the MPD thrusters, e.g., in Tobari et al. (2007). Two dimensional measurement of the plasma-induced axial magnetic field has been performed in some experiments (Roberson et al. 2011; Corr and Boswell 2007; Takahashi et al. 2016; Shinohara et al. 2016) and shows the negative value of the change of the axial magnetic field ($\Delta B_z < 0$), being consistent with the electron-diamagnetic model. The

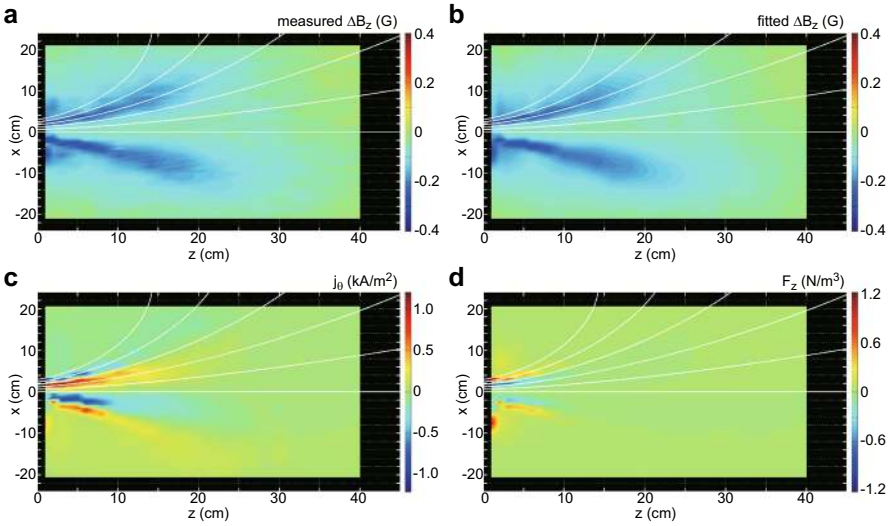

Fig. 15 x-z profiles of **a** the measured plasma-induced magnetic field strength ΔB_z, **b** the fitted data of **a**, **c** the calculated azimuthal electric current density j_θ induced by the plasma, and **d** the axial Lorentz force density F_z calculated from j_θ in **c** and the profile of the radial magnetic field B_r in the helicon thruster 'HPT-I'. Figure is taken from Takahashi et al. (2016)

azimuthal electric current $\mathbf{J}_\mathrm{p}$ is obtained from $\nabla \times \mathbf{B} = \mu_0 \mathbf{J}_\mathrm{p}$, where the azimuthal component can be written as

$$J_\theta = \frac{1}{\mu_0}\frac{\partial \Delta B_\mathrm{r}}{\partial z} - \frac{1}{\mu_0}\frac{\partial \Delta B_z}{\partial r} \sim -\frac{1}{\mu_0}\frac{\partial \Delta B_z}{\partial r}. \tag{25}$$

The relation of $\partial \Delta B_\mathrm{r}/\partial z \ll \partial \Delta B_z/\partial r$ was confirmed in the experiment (Takahashi et al. 2016). The two-dimensional profile of the plasma-induced current j_θ can be obtained as seen in Fig. 15. This current is in fair agreement with the sum of the electron-diamagnetic drift current and the Hall current ($\mathbf{E} \times \mathbf{B}$ drift current of the electrons) for all the magnetic field strength tested there, i.e., the current given by

$$j_\theta = \frac{1}{B_z}\frac{\partial p_\mathrm{e}}{\partial r} + e n_\mathrm{p}\frac{E_\mathrm{r}}{B_z}. \tag{26}$$

It should be noted that the current was calculated from the profiles of the plasma density, the electron temperature, and the plasma potential measured by the Langmuir probe. The result has shown that the azimuthal current is still in fair agreement with the electron–diamagnetic drift current for the typical magnetic field rather than the electron Hall current; meaning the major contribution of the electron-diamagnetic current on the T_B term. This fact implies that the electron pressure in the magnetic nozzle is mainly balanced with the magnetic pressure force, rather than the electrostatic force, indicating the validity of the simplified electron-diamagnetic thruster models (Fruchtman 2006; Takahashi et al. 2011b; Fruchtman et al. 2012).

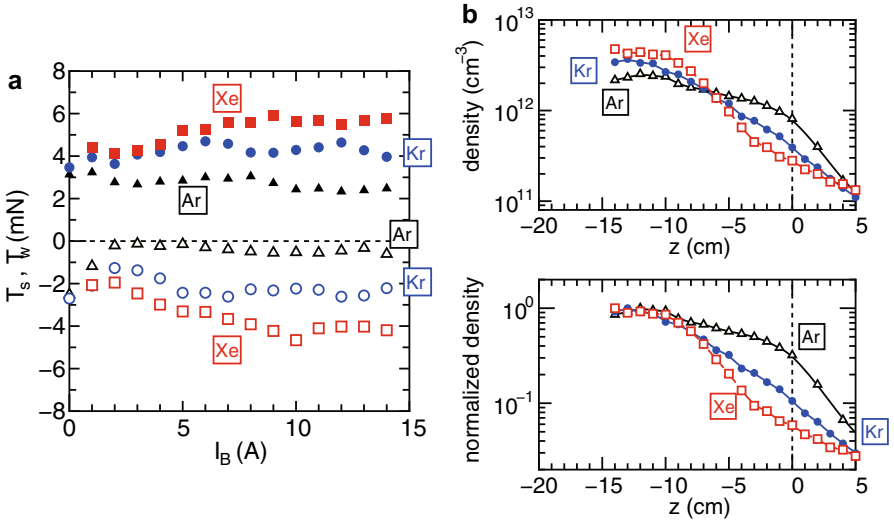

Fig. 16 Measured axial force to the back plate (T_s; filled symbols) and to the radial wall (T_w; open symbols) as functions of the solenoid current I_B for argon (triangles), krypton (circles), and xenon (squares). **b** Axial profiles of the plasma density and the normalized density for argon (open triangles), krypton (filled circles), and xenon (open squares), together with the lines added as visual guides. Figure is taken from Takahashi et al. (2015)

5.5.3 Axial momentum lost to the wall

Modeling of the plasma production region is also crucial to design the thruster, where some studies analyzed the momentum balance, the energy balance, or both in the source cavity, and gave the plasma parameters in the source; then the obtained parameters were connected to the magnetic nozzle region with the given plasma injection at the nozzle entrance (Lafleur 2014; Ahedo and Navarro-Cavallé 2013; Takahashi et al. 2016). The model of the plasma production is also related with the cross-field plasma diffusion (Fruchtman 2009) and the threshold of the magnetic field strength for efficient transport of the plasma to the source exit was experimentally observed (Little and Choueiri 2015). One of the thruster models has identified that the inefficient thruster performance results from the energy loss to the radial source wall (Lafleur 2014). The ions lost to the radial wall generally have both the radial and axial components (of course, azimuthal one, too) of the momentum flux ($m_i n_w u_{rw}^2$ and $m_i n_w u_{rw} u_{rz}$). The ions near the radial wall were assumed to be axially slow and not to deliver significant axial momentum to the radial wall in the one-dimensional models (Fruchtman 2008a). Even in two-dimensional model giving the plasma parameters in the source, the momentum balances in the radial and axial directions have been decoupled by neglecting the radial variation of the axial momentum (Ahedo and Navarro-Cavallé 2013), which corresponds to the radially lost flux of the axial momentum and to the T_w term shown in Eq. (20). However, a non-negligible axial force to the radial source wall T_w has been detected as shown in Fig. 16a when the propellant gas is changed to krypton and xenon, where the highly

ionized plasma is produced inside the source (Takahashi et al. 2015). Simultaneously with the negative T_w force, a rapid decay of the plasma density along the axis is observed inside the source tube as in Fig. 16b. The axial non-uniformity of the density along the axis is induced by the neutral depletion phenomenon, which is described in the next section in more detail. The strong density gradient inside the source develops the axial electric field in the plasma core and accelerates the ions, i.e., the electron pressure is converted into the axial ion dynamic momentum (Takahashi and Ando 2017). When these accelerated ions are lost to the wall, they seem to deliver significant axial momentum flux to the radial wall as sketched in the inset of Fig. 6a. Therefore, the previously neglected axial momentum lost to the radial wall has also to be incorporated, especially for high-power operation of the helicon thruster involving the neutral depletion. The negative T_w term was also confirmed by a PIC simulation (Takao and Takahashi 2015), where the neutral is artificially depleted to reproduce the neutral depletion and the momentum flux to the radial source wall was numerically calculated.

The thrust generation and loss mechanisms briefly understood in the above-mentioned studies will give insight into improvement of the thruster performance; the inhibition of the plasma loss to the radial wall is one of the key issues. For improvement of the helicon plasma thruster performance, a stepped-diameter source tube was also tested (Takahashi et al. 2018) where the radial source wall is separated from the magnetic field lines by enlarging the source diameter near the thruster exit and very similar to the conical helicon thruster (Charles et al. 2012); a slight increase in the thrust was observed, which seems to originate from the geometrical separation of the plasma from the radial source wall.

5.6 Plasma–neutral interaction

For the high-power operation of any plasma sources, a number of laboratory experiments have shown that plasma–neutral interactions significantly affect plasma dynamics, especially neutral depletion phenomena have appeared (Degeling et al. 1999; Yun et al. 2000; Keesee and Scime 2006; Aanesland et al. 2007; Shimada et al. 2007; Keesee and Scime 2007; O'Connell et al. 2008; Denning et al. 2008; Magee et al. 2013). One of the early experiments has observed the oscillation of the plasma density due to the neutral depletion or neutral pumping phenomenon (Degeling et al. 1999). The plasma–gas interaction dynamics seem to be very similar to the ionization oscillation in the Hall thruster operated for the high electric power. In the high-power ECR plasmas, interesting structural formations have also been observed, some of which seem to be induced by a plasma–gas interaction, such as an anti $\mathbf{E} \times \mathbf{B}$ drift of the ions induced by the momentum transfer from the neutral pressure gradient (Okamoto et al. 2003). Analytical models gave findings on plasma transport modified or enhanced by the neutral depletion (Fruchtman et al. 2005, 2008; Liard et al. 2007; Fruchtman 2008a, b, 2010). Especially, the plasma density profile has an upstream density peak when introducing the gas from the upstream port of the source having the downstream open source exit, which is simulating the thruster in space (Fruchtman 2008a). Furthermore, reproduction of the neutrals can

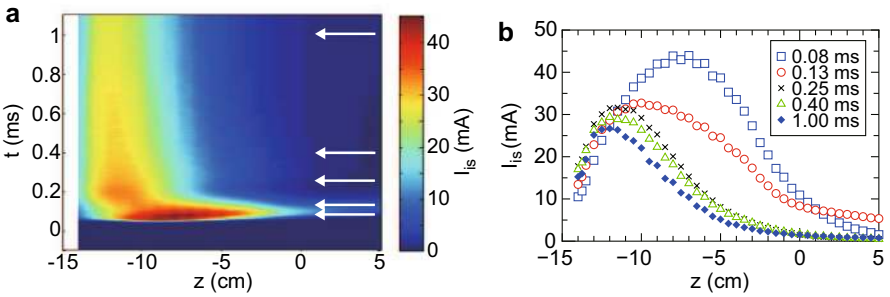

Fig. 17 **a** Spatiotemporal (z–t) evolution of the ion-saturation current I_{is} of the Langmuir probe, being proportional to the plasma density, where the helicon plasma source is pulsed after introducing the propellant argon continuously. **b** Axial profiles of the ion saturation current I_{is} at the representative times shown by the solid arrows in **a**. Figure is taken from Takahashi et al. (2016)

occur at the wall when the ions are lost to and recombined at the wall (Ahedo and Navarro-Cavallé 2013; Fruchtman et al. 2008), which affects the density profile inside the source and the plasma ejection to the magnetic nozzle region. Therefore understanding the plasma–neutral interaction and its control are also key issues to improve the thruster performance hereafter, being related to the plasma transport in the source and the momentum loss to the wall.

Temporally relative value of the neutral density was estimated from the time-resolved optical emission in the pulsed helicon thruster immersed in vacuum, where the gas was continuously introduced and only the rf power is pulsed (Takahashi et al. 2016). The rapid decrease in the neutral density was detected and about 80% of the neutral seems to be depleted near the thruster source exit. This depletion is considered to be due to the local ionization of the neutrals; the profile of the plasma density has a peak near the thruster exit at the initial time of the discharge. The peak of the plasma density was subsequently observed to shift to the upstream side inside the source tube as seen in the spatiotemporal evolution of the plasma density in Fig. 17. In the vacuum tube located in the chamber evacuated by a high-speed pumping system, the neutral density profile is generally non-uniform, as Giannelli et al. analyzed the pressure distribution of the neutral pressure in a helicon source tube (Giannelli et al. 2013). Their analysis has shown that the maximum density is located near the gas injection port located upstream of the source as expected easily. To inhibit the axial momentum lost to the radial wall due to the neutral-depletion-induced upstream density peak, a configuration having the gas injection port near the source exit has been tested (Takahashi et al. 2016). The experimental result shows the increase in the imparted thrust and the density downstream of the source by about 25–40%; the upstream density peak seems to be inhibited for the downstream gas injection case. This result shows that the non-uniform profile of the plasma density induced by the neutral profile significantly affects the performance of the helicon thruster. The gas injection port located near the source tube exit has also similarly been tested in a helicon source attached to the diffusion chamber and the local peak of the plasma density

is formed near the gas injection port (Shinohara et al. 2019). The optimization will be required in near future and a simulation will be a powerful tool for designing the thruster configuration. Actually, a PIC simulation coupled with a Direct Simulation Monte Carlo (DSMC) code was performed for the helicon thruster, which has shown a qualitatively consistent result with the experiments (Takase et al. 2018).

Addressing the plasma–gas interaction more, the charge-exchange collision is one of the important collisional processes to dominate the mean ion velocity, where the charge exchange works as a drag force on the ion flow since the charge-exchange collision generally produces the slow ions and the high-speed neutrals. However, the charge-exchange collision itself does not change the total momentum (including the neutral momentum) according to the momentum conservation's law. Makrinich and Fruchtman have proposed that the momentum gain can be increased if the mean-free path of the ion-neutral charge-exchange collision is shorter than the scale length of the potential drop (Fruchtman 2014, 2011; Makrinich and Fruchtman 2009). Lukas et al. proposed the application of this concept to high thrust-to-power ratio micro-cathode arc thruster (Lukas et al. 2016). For more high-neutral density regime, the neutral gas is efficiently heated due to the neutral–neutral collisions. The neutral heating process is suggested to be used for another type of the electric propulsion device named the 'pocket rocket' (Boswell et al. 2011; Charles et al. 2014). The detailed physical mechanisms of the plasma–neutral interaction in various regimes have been discussed in Fruchtman (2017).

As briefly described above, the plasma dynamics in the helicon thruster are sometimes affected by the plasma–neutral interaction; it is important to understand its effects on various phenomena occurring in thrusters.

5.7 Electron thermodynamics in the magnetic nozzle

In the helicon thruster consisting of the negligible ion temperature and the finite electron temperature, the thermodynamic property of the electrons is very important and affects the thruster performance. Especially, the electron cooling during the magnetic expansion is crucial for the thruster performance, since the energy source of the thrust imparted by the helicon thruster is the electron internal energy. Arefiev and Breizman analyzed the adiabatic electron cooling with the presence of the ambipolar electric field in the magnetic nozzle (Arefiev and Breizman 2008). More simply, the thermodynamic behavior, i.e., the energy interaction between the surroundings, can be very briefly characterized by a polytropic index γ as

$$pV^{\gamma} = \text{const}, \tag{27}$$

where p and V are the pressure and the volume, respectively. The value of γ is equal to unity for the isothermal expansion, equal to infinity for isometric expansion, and equal to the specific heat ratio γ_a for the adiabatic expansion, i.e., $\gamma = \gamma_a = (N_d + 2)/N_d$, where N_d, the number of degrees of freedom, is 3 for monoatomic ($\gamma_a = 5/3$). The polytropic relation can be rewritten using the normalized density n/n_0 and the normalized temperature T/T_0 as

$$\frac{T}{T_0} = \left(\frac{n}{n_0}\right)^{\gamma-1}. \tag{28}$$

This value is sometimes coupled with the fluid equations to obtain the self-consistent plasma solution. The first law of thermodynamics is that the change in the internal energy of a close system (ΔU) is equal to the added heat (Q) plus the net work (W) to the system by the surroundings:

$$\Delta U = Q + W. \tag{29}$$

For an expanding system, the work W can be expressed by the pressure and the change in the volume ΔV;

$$\Delta U = Q - p\Delta V. \tag{30}$$

The isothermal, isometric, and adiabatic expansions correspond to the cases of $\Delta U = 0$, $\Delta V = 0$, and $Q = 0$, respectively. The polytropic relation in Eqs. (27) and (28) and the first law of thermodynamics in Eqs. (29) and (30) well describe the change in the internal energy, the added work, and the heat transfer between surroundings, identifying the polytropic index is indeed important to the characterize the energy interaction with the surroundings during the plasma expansion. For example, estimation of the electron polytropic index from the observation near the Sun and the Earth have been used to model the plasma-expansion process. Some of the data have been interpreted as demonstrating that the solar wind expands isothermally, rather than adiabatically, implying the presence of the heating source of the plasma in interplanetary space (Doorsselaere et al. 2011; Jacobs and Poedts 2011; Retinó 2016). In previous thruster models, the thruster performance has also been analyzed with the momentum equations coupled with the polytropic relation, where the polytropic index γ was treated as a control parameter or the previously measured value was used (Lafleur et al. 2015; Merino and Ahedo 2016). Laboratory experiments under adiabatic conditions (no heating source) have shown a nearly isothermal polytropic index of $\gamma \sim 1$–1.2 in the magnetic nozzle (Sheehan et al. 2014; Zhang et al. 2016; Little and Choueiri 2016). Little and Choueiri established a model giving the nearly isothermal polytropic index, where high heat conductivity for electrons was assumed. In their model, the coupling between the electrons and ions is weak, so that the ions do not gain energy in the magnetic nozzle. In both the model and experiment, the Maxwellian EEPFs are assumed based on the facts that it was performed in the large-scale chamber and with the high plasma density. However, it is rarely Maxwellian in low-pressure, non-equilibrium, laboratory plasmas as observed in a number of experiments, while the precise measurement of the EEPF has not been successfully performed in Little and Choueiri (2016). Even in the non-Maxwellian EEPFs, the nearly isothermal polytropic index $\gamma \sim 1.17$ has been obtained, but it strongly depends on the shape of the EEPFs (Zhang et al. 2016), which is affected by a non-local effect of the ambipolar, CFDL, and sheath electric fields as demonstrated by the detailed axial measurement of the EEPFs (Takahashi et al. 2007; Boswell et al. 2015). It should be mentioned that the electrons are well known to be nearly isothermal in low-pressure laboratory plasmas, when they are

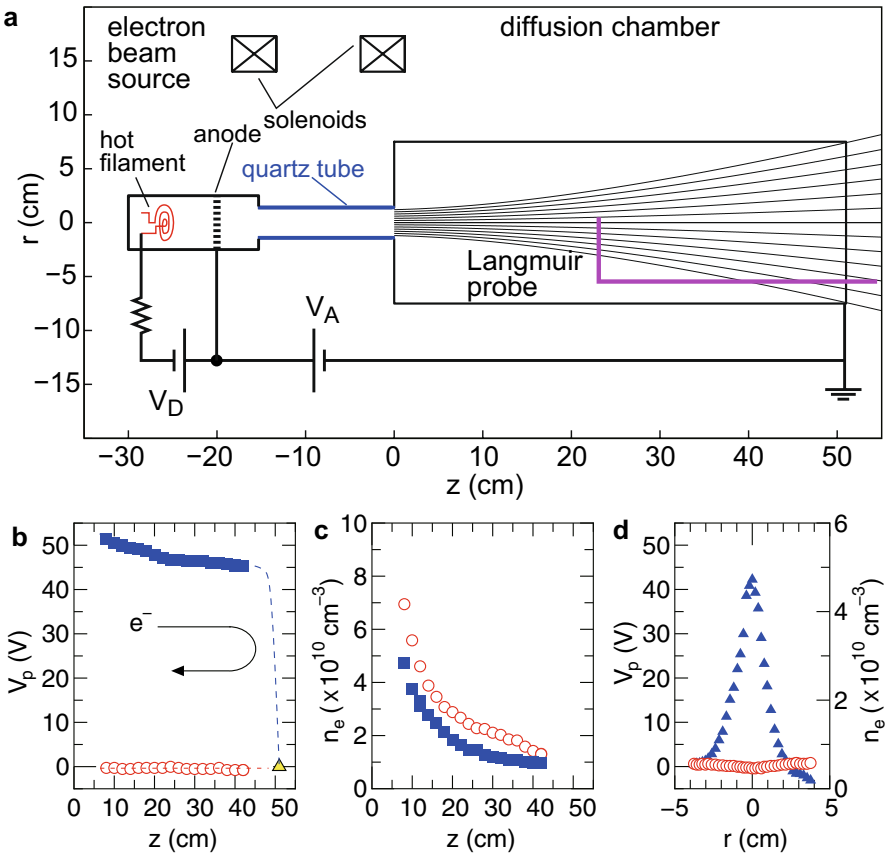

Fig. 18 **a** Schematic diagram of the experimental setup yielding the zero- and high-potential plasmas in the magnetic nozzle. Axial profiles of **b** the plasma potential and **c** the electron density along the axis for the high ($V_A = 60$ V; filled squares) and zero ($V_A = 0$ V; open circles)-potential plasmas. **d** Radial profile of the plasma potential (open circles) and the electron density (filled triangles) for the $V_A = 0$ V case. Figure is taken from Takahashi et al. (2018)

trapped in the system by the electric fields. However, both the electrons trapped in and escaping from the system coexist as observed as a depleted tail in the EEPFs in numerous laboratory experiments (Kortshagen et al. 1994; Godyak et al. 1995; Takahashi et al. 2007, 2011). Then a very simple question arises: *what would happen if there were no electric fields trapping the electrons?* Furthermore, when the electron cooling (corresponding to the decrease in the internal energy: $\Delta U < 0$) occurs during the magnetic nozzle expansion, the electrons have to do work on somewhere and somehow if the first law of thermodynamics is valid in the collisionless system.

Two interesting experiments relating to the electron thermodynamics in the magnetic nozzle were performed in 2018 and similar conclusions on the polytropic index of the free electrons were obtained (Takahashi et al. 2018; Kim et al. 2018).

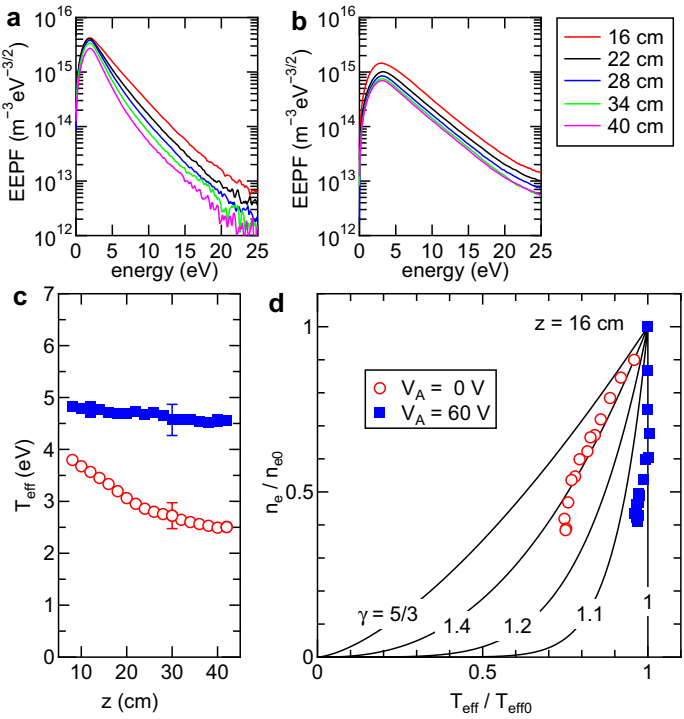

Fig. 19 EEPFs in the energy range less than 25 eV showing only the thermalized electrons for **a** the zero-potential plasma case ($V_A = 0$ V) and **b** the high-potential plasma ($V_A = 60$ V) cases. **c** Axial profile of the effective electron temperature T_{eff} obtained by integrating the EEPFs with the energy less than 25 eV for $V_A = 0$ V (open circles) and $V_A = 60$ V (filled squares). **d** Polytropic relation obtained from the normalized electron density n_e/n_{e0} and effective electron temperature T_{eff}/T_{eff0}, together with the theoretical curve given by Eq. (28) for various values of the polytropic idex γ. Figure is taken from Takahashi et al. (2018)

Takahashi et al. successfully removed all the electric field from the system or generate a high-potential plasma in the specially constructed setup shown in Fig.18a, where the filamented argon plasma source is connected to the diffusion chamber via a quartz tube, which isolates the grounded chamber and the source electrically, and biased at a controlled voltage V_A. The measured profiles of the plasma potential show the zero electric field for $V_A = 0$ V while maintaining the density gradient, and the high plasma potential resulting from the ambipolar and sheath electric fields for $V_A = 60$ V as in Fig. 18b–d. For the $V_A = 0$ case, an electron current can be injected into the diffusion chamber region in addition to the plasma diffusion, yielding the decrease in the plasma potential. The spontaneous electric field such as the sheath and the ambipolar electric field can be removed by compensating the space charge with the injected electrons. In the zero-electric-field situation, the electrons injected from the plasma source interact only with the magnetic nozzle and never back to the source, while the electrons can be trapped by the sheath for the high-potential case. Kim et al. have independently measured the trapped and free electrons using

a Langmuir probe having two tips facing upstream and downstream. These two different experimental approaches surprisingly gave the similar considerations that the trapped electrons are isothermal ($\gamma \sim 1$) as described in the textbook, while the free electrons escaping from the system are nearly adiabatic showing the value of γ approaching 5/3, as shown by the measurements for $V_A = 60$ V and $V_A = 0$ V cases in Fig. 19 (Takahashi et al. 2018). These imply that the magnetic nozzle can work as a nearly perfect adiabatic wall for the electron gas and the pressure force of the electron gas does work on the magnetic wall, while the isotherm-like observations seem to be due to the presence of the electric field trapping the electrons within the system. The adiabatic thermodynamic property is indeed consistent with the physical description of the electron-diamagnetic-induced thrust model, which does work on the magnetic nozzle via a Lorentz force arising from the azimuthal diamagnetic current and the radial magnetic field (Takahashi et al. 2011b, 2013a). This can also be interpreted as the magnetic field modification induced by the internal current of the plasma (Takahashi et al. 2016). Furthermore it is also consistent with the one-dimensional magnetic nozzle model being equivalent to the physical nozzle model, where the electron pressure does work on the wall surface (Fruchtman et al. 2012). Actually, thruster experiments have detected the spatial displacement of the magnetic nozzle by the axial electron-diamagnetic force. This implies that the internal energy of the electron gas is converted into the mechanical energy of the nozzle structure by doing work on the magnetic nozzle.

If the magnetic nozzle thruster is operated in space, there is no sheath downstream of the magnetic nozzle. However, the system will still have the ambipolar electric field which will confine the electrons in the system and the voltage would be close to the value obtained from the current-free condition as in Eq. (24). Hence, it would be expected that the EEPF is non-Maxwellian due to the low collisionality in the low-density magnetic nozzle plasmas and the non-local effect. An effective polytropic index of the electrons in the magnetic nozzle plasma thruster still seems to be an open question in such a situation and the experiments over the wide range of the parameters would be interesting.

5.8 Plasma detachment from the magnetic nozzle

After various momentum conversion and acceleration processes occur in the expanding magnetic field, one will come across the biggest problem in the magnetic nozzle thruster: plasma detachment from the magnetic nozzle as seen in Fig. 1c. The magnetic field lines of the magnetic nozzle form a closed structure according to $\nabla \cdot \mathbf{B} = 0$; hence it surely turns back to the thruster. The plasma flow has to be detached from the magnetic field lines and be exhausted from the system into the space, otherwise no net thrust will be obtained when all the plasma turns back to the thruster along the closed field lines. In typical thruster configuration, the ions are unmagnetized due to their Larmor radius and expected to be easily detached from the magnetic field lines. Two-dimensional characterization of the ion beam accelerated by the CFDL has shown the deviation of the ion beam radius from the expanding radius expected from the magnetic field profile, where the ion beam radius

slightly expands along the magnetic field near the thruster exit and deviation was detected at about 10 cm downstream of the source (Takahashi et al. 2011). Cox et al. estimated the divergence angle of the ion beam as about 20° at the beam edge (Cox et al. 2008). Takahashi et al. has observed the collimated and divergent ion beams generated by the plane and hemispherical potential structures near the thruster exit for the low and high gas pressure condition, respectively (Takahashi and Fujiwara 2009; Takahashi et al. 2010). Winglee et al. have observed the collimated plasma beam when adding an additional solenoid to the high-power helicon thruster operated at about a few tens of kW (Winglee et al. 2007). Deline et al. have observed the deviation of the plume radius, which was produced by a high-power pulsed dc plasma gun, from the magnetic field lines (Deline et al. 2009). Terasaka et al. also showed the detachment of the ion streamline from the magnetic field lines, where the local mean velocity vector is measured by a Mach probe (or a directional Langmuir probe) calibrated with the LIF method (Terasaka et al. 2010). VASIMR experiment has similarly shown the deviation of the ion-density profile from the magnetic field lines (Olsen et al. 2015). All of the above-mentioned experiments evaluated the profile or velocity of the ions in plasmas and it can be concluded that the ion detachment can occur in the magnetic nozzle as analyzed by a particle orbit calculation excluding electron dynamics (Gesto et al. 2008). Once the ions are detached from the magnetic field lines and the electrons are still magnetized, the charge separation will develop the electric field pulling back the ions to the thruster. Actually, the experiment performed by Terasaka et al. has shown the formation of the electric field simultaneously with the ion streamline detachment and the resultant rotation of the ions (Terasaka et al. 2011).

To overcome the issue on the detachment of the electrons, several models have been proposed for the last quarter century. Hooper proposed the detachment model taking the ambipolar drift of a two-fluid plasma across the magnetic field lines, where the electron drift velocity perpendicular to the magnetic field is approximately given using a hybrid ion-electron Larmor radius as

$$\frac{v_{e\perp}}{u} \sim \frac{m_e u}{eB}\frac{m_i u}{eB}\frac{1}{R_c^2}, \tag{31}$$

where $v_{e\perp}$, u, and R_c are the electron drift velocity perpendicular to the magnetic fields, the ion drift velocity, and the curvature radius of the magnetic field line, respectively (Hooper 1993). This model is further extended to include non-zero angular velocity injection by Schmit and Fisch (2009). More recently, Ahedo and Merino claimed that this detachment scenario is the outward plasma diffusion from the magnetic-nozzle-guided plasma flow. They analyzed the model considering the electron and ion-fluid equations without assuming a local current ambipolarity (Ahedo and Merino 2011; Merino and Ahedo 2014). The brief results implied the detachment scenario of the ions via their demagnetization in the nozzle, while the electron pressure is balanced with the electrostatic force, rather than the magnetic force, when decreasing the magnetic field strength in the downstream side of the magnetic nozzle. A turbulence-induced anomalous cross-field diffusion of the electrons has been discussed based on the VASIMR experiments (Olsen et al. 2015).

These detachment scenarios are essentially based on the ambipolar diffusion across the magnetic field lines.

The other scenario is a magnetohydrodynamic (MHD) plasma detachment from the magnetic nozzle suggested by Arefiev and Breizman (Arefiev and Breizman 2005; Breizman et al. 2008). Their model proposed that the plasma flow can stretch the magnetic field lines to infinity and the plasma flow can be detached from the magnetic nozzle. Their theory predicted that the stretch of the magnetic nozzle can occur when the plasma flow velocity exceeds the Alfvén velocity $V_A = B_z/\sqrt{\mu_0 m_i n_p}$ calculated from the vacuum magnetic field strength B_z, i.e., in super-Alfvénic regime ($M_A > 1$, where $M_A \equiv u_z/V_A$ with the plasma flow velocity u_z), where μ_0 is the magnetic permeability. This is indeed similar to the Alfvén's frozen-in theorem. The similar phenomenon can be frequently seen in space plasmas and astrophysical objects, e.g., a geomagnetotail modified by the solar wind, the plasma ejection from the Sun, the astrophysical jet, and so on (Parker 1958; Mikic et al. 1988; Usadi et al. 1993; Kato et al. 2004). An experiment performed by Deline et al. has shown the

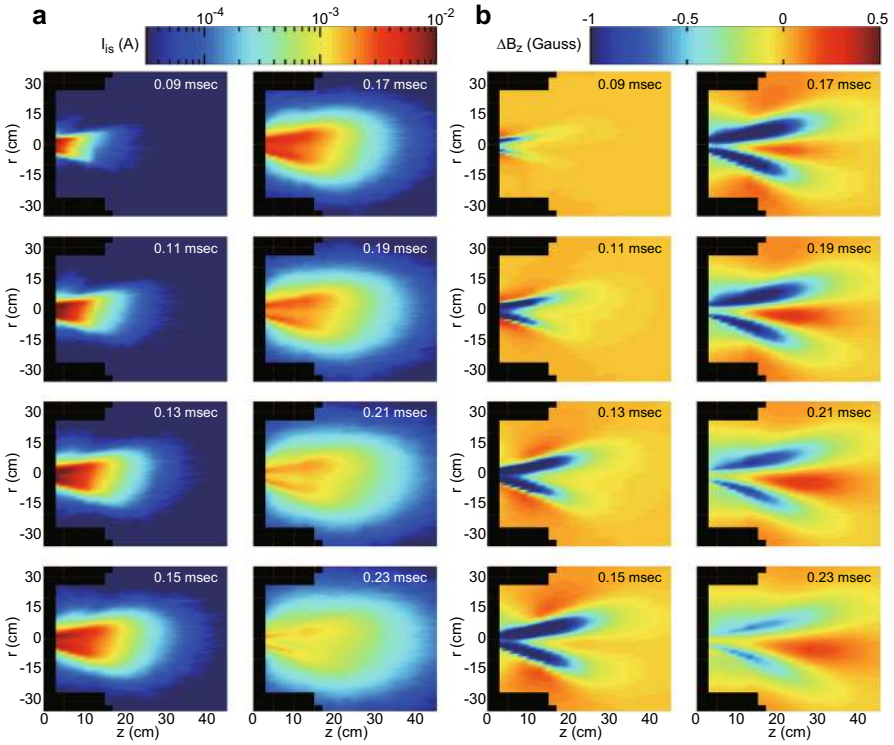

Fig. 20 Spatiotemporal evolution of **a** the ion saturation current I_{is} and **b** the plasma-induced axial magnetic field ΔB_z, taken for $I_B = 4.5$ A and $P_{rf} = 5$ kW. The rf power is turned on at $t = 0$ and the signals are taken at various probe locations, where the measurements are performed at about 20 points along z and 60 points along r; hence total measurement points are about 1200 points. The signals are averaged over 16 shots at each probe location. A movie can also be found as a supplemental material in Takahashi and Ando (2017). Figure is taken from Takahashi and Ando (2017)

deviation of the plume radius from the magnetic nozzle at the axial location giving $M_A = 1$, whereas the measurement of the plasma-induced magnetic fields has not been performed (Deline et al. 2009). Previous laboratory experiments in low-temperature plasmas have typically shown the diamagnetic signals showing the decrease in the axial magnetic fields ($\Delta B_z < 0$), which diverges the magnetic nozzle rather than stretches it (Stenzel and Urrutia 2000; Corr and Boswell 2007). Although the plume deviation from the magnetic nozzle observed by Winglee et al. was discussed with the MHD scenario (Winglee et al. 2007), their subsequent experiment showed the strong diamagnetic feature downstream of the high-power helicon plasma source (Roberson et al. 2011), showing the inconsistency. These diamagnetism are consistent with the electron-diamagnetic-induced thrust model and experiments, since the azimuthal current loop generating the magnetic field opposite in direction to the applied field can be forced toward the downstream direction as demonstrated by Takahashi et al. (Takahashi et al. 2011b, 2012, 2013a, 2016).

To verify the MHD detachment scenario, detailed measurement of the plasma-induced magnetic fields ΔB_z was carried out in a helicon plasma thruster operated at pulsed rf power up to 5 kW (Takahashi and Ando 2017), where the high-density plasma is sustained only for an initial hundred of μs of the discharge due to the neutral depletion as shown in Takahashi et al. (2016). The spatiotemporal evolutions of the ion saturation current I_{is} and the plasma-induced axial magnetic field ΔB_z are shown in Fig. 20. The two-dimensional measurements showed that the diamagnetic signal ($\Delta B_z < 0$) near the thruster exit, being consistent with the thrust generation in the magnetic nozzle, while the increase in the magnetic field ($\Delta B_z > 0$) corresponding to the stretch of the magnetic nozzle was observed more downstream of the magnetic nozzle when the plasma flow reaches the downstream side (it is clearly seen around $t \sim 0.2$ ms and disappears after that due to the temporal decrease in the density). The condition giving the transition of the plasma flow state from diverging to stretching the magnetic nozzle was experimentally investigated by changing the plasma density (the

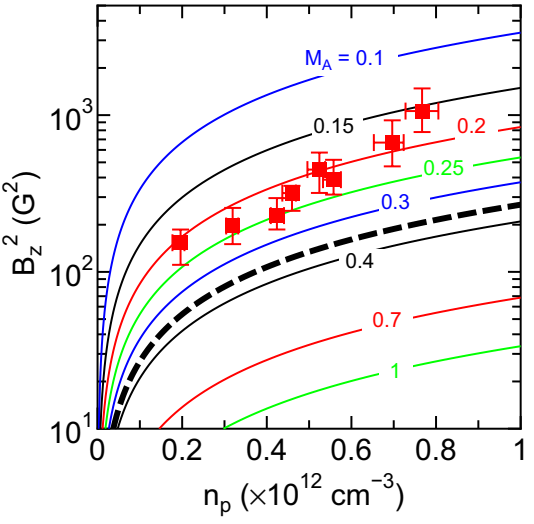

Fig. 21 Measured plasma density n_p and the square of the applied magnetic field strength B_z at the transition positions from the diverging-to-stretching states. The solid lines correspond to the various Alfvén Mach number M_A labeled in figure. The bold dashed lines can be obtained from Eq. (36), where the measured values of $v = 2$ km/s and $T_e = 5$ eV are used for the calculation. Figure is taken from Takahashi and Ando (2017)

rf power) and the magnetic field strength (the solenoid current), where the transition position is clearly seen to be changed by these parameters. The magnetic field strength and the density at the transition positions are plotted in n_p–B_z^2 plane by filled squares as in Fig. 21, together with the calculated curves for various values of the Alfvén Mach number M_A. The result shows that the transition can occur at the axial location where the Alfvén of $M_A \sim 0.2$–0.25, which is more upstream than the previous model. This was qualitatively and very briefly discussed in the MHD equilibrium model (Takahashi and Ando 2017) and described in more detail as follows, while the detailed numerical calculation has not been done yet.

The steady-state momentum equation in an ideal MHD approximation is

$$\rho(\mathbf{v}\cdot\nabla)\mathbf{v} = -\nabla p - \nabla B^2/2\mu_0 + (\mathbf{B}\cdot\nabla)\mathbf{B}/\mu_0, \tag{32}$$

where ρ and p are the mass density ($\sim mn_p$) and the pressure ($\sim n_p k_B T_e$), respectively. The last two terms on the right-hand side are the magnetic pressure and tension terms, respectively, which are derived from the $\mathbf{J}\times\mathbf{B}$ term and Ampere's law. It should be noted that the magnetic field B is not the vacuum magnetic field but the total magnetic field consisting of the applied and plasma-induced magnetic fields ($\mathbf{B} = \mathbf{B}_v + \Delta\mathbf{B}$). Here very rough dimension analysis was considered to understand the physics for three cases including two extreme conditions of the upstream and downstream of the magnetic nozzle.

(1) Upstream limit of the magnetic nozzle

When assuming a static plasma with no flow velocity and a uniform axial magnetic field, corresponding to the upstream side of the magnetic nozzle, Eq. (32) gives the well-known pressure equilibrium as

$$\nabla\left(p + \frac{B^2}{2\mu}\right) = 0, \tag{33}$$

$$p + \frac{B^2}{2\mu} = \frac{B_v^2}{2\mu}, \tag{34}$$

where the inertia term of the left-hand side (LHS) and the tension term of the RHS in Eq. (32) are negligible. This means that the total axial magnetic field is reduced in the plasma core when the plasma has a finite pressure p, being equivalent to the negative ΔB_z and to the presence of the diamagnetic plasma current. Hence this consideration can well explain the negative ΔB_z near the thruster exit.

(2) Downstream limit of the magnetic nozzle

At the downstream limit of the magnetic nozzle, the magnetic field strength decreases and the field lines diverge; the plasma flow velocity is large and the pressure is small. In this situation, both the plasma and magnetic pressure terms in Eq. (32) can be neglected. The dimension analysis was carried out, assuming the scale length L of the gradient of the physical parameters, i.e., $|\nabla| \sim 1/L$, being often

used for considering the physics qualitatively (Davidson 2001). Then Eq. (32) gives the equilibrium condition as

$$v^2 \simeq v_{\mathrm{A}}^2 = \frac{B^2}{\mu\rho} = \frac{(B_v + \Delta B)^2}{\mu\rho}. \tag{35}$$

This implies that the velocity v cannot exceed the Alfvén velocity calculated from the total magnetic field. In other words, the plasma flow can increase the magnetic field ($\Delta B_z > 0$) or can stretch the magnetic nozzle when the flow velocity exceeds the Alfvén velocity ($M_{\mathrm{A}} > 1$) calculated from the vacuum magnetic field strength. This is very similar to the frozen-in theorem or the model proposed by Arefiev and Breizman (2005).

(3) Intermediate situation

Finally, let us consider the intermediate condition between the cases 1 and 2, where all the terms in Eq. (32) are non-negligible, being close to the experimental conditions. The same dimension analysis procedure gives the equilibrium condition as (Takahashi and Ando 2017)

$$v^2 \simeq \frac{V_{\mathrm{A}}^2}{2} - C_{\mathrm{s}}^2 = \frac{B^2}{2\mu\rho} - C_{\mathrm{s}}^2 = \frac{(B_v + \Delta B)^2}{2\mu\rho} - C_{\mathrm{s}}^2, \tag{36}$$

where C_{s} is the ion sound speed given by $C_{\mathrm{s}} = \sqrt{k_{\mathrm{B}} T_{\mathrm{e}}/m_{\mathrm{i}}}$. This indicates that the magnetic field lines are stretched when the square of the flow velocity exceeds $B_v^2/2\mu\rho - C_{\mathrm{s}}^2$. This equilibrium condition is over-plotted in Fig. 21 by a bold dashed line, showing the transition occurring for $M_{\mathrm{A}} \sim 0.3$–0.4 and qualitatively explaining the plasma-flow-state variation from diverging to stretching the magnetic nozzle, occurring for $M_{\mathrm{A}} < 1$. This result is significant first step toward the MHD plasma detachment, although the change in the magnetic field strength is only a few percent of the applied field.

As described above, a number of theories, experiments, and discussions have been made over the past several decades. However the mechanisms of the plasma detachment are still in argument and its effect on the thruster performance is not understood yet.

6 Thruster assessments, peripheral components, and a new application to space debris removal

In the first direct measurements of the thrust reported by Pottinger et al. (2011) and Takahashi et al. (2011a), the thrusts are only a few mN for about 1 kW rf power for both the experiments. The performance has gradually and steadily been improved via the above-described fundamental studies. In this section, the typical results on the thruster assessment are reviewed. Furthermore, the studies useful for the thruster design including peripherals such as permanent magnet configurations for the magnetic nozzle, rf power generators, impedance matching circuits, are described.

Table 1 Typical results on the assessment of the rf magnetic nozzle thrusters, where the results except for Kuwahara et al. (2017) were measured using thrust stands

Publications	P_{rf} (kW)	F (mN)	I_{sp} (s)	F/P_{rf} (mN/kW)	η_{rf} (%)	Gas
1-Takahashi et al., APL2011 (Takahashi et al. 2011a)	0.9	3	510	3.3	0.83	Ar
2-Pottinger et al., JPD2011 (Pottinger et al. 2011)	0.65	2.8	286	4.3	0.6	Kr
3-Takahashi et al., PRL2011 (Takahashi et al. 2011b)	0.8	6	816	7.5	3.0	Ar
4-Charles et al., APL2012 (Charles et al. 2012)	0.8	5	680	6.3	2.1	Ar
5-Takahashi et al., PRL2013 (Takahashi et al. 2013a)	1	11	1559	11.0	8.4	Ar
6-Shabshelowitz and Gallimore, JPP2013 (Shabshelowitz and Gallimore 2013)	1.5	11	160	7.33	0.58	Ar
7-Williams and Walker, JPP2013 (Williams and Walker 2013)	0.6	6	136	10	0.67	Ar
8-Takahashi et al., JPD2013 (Takahashi et al. 2013b)	2	15	2126	7.5	7.8	Ar
9-Charles et al. APL2013 (Charles et al. 2013)	0.9	6	696	6.7	2.3	Xe
10-Harle et al. PSST2013 (Harle et al. 2013)	0.4	1.1	187	2.75	0.25	Ar
11-Takahashi et al. PSST2014 (Takahashi et al. 2014)	2	20	2721	10	13.3	Ar
12-Takahashi et al. PSST2015 (Takahashi et al. 2015)	6	58	2818	9.7	13.3	Ar
13-Kuwahara et al. JPP2017 (Kuwahara et al. 2017)	3	40	459	13.3	3.0	Xe
14-Oshio et al. IEPC2017 (Oshio et al. 2017)	1	6	510	6.0	1.5	Ar
15-Siddiqui et al. IEPC2017 (Siddiqui et al. 2017)	0.1	5	146	50	3.6	Xe
16-Trezzolani et al. IEPC2017 (Trezzolani et al. 2017a)	0.15	1.4	714	9.33	3.3	Xe
17-Trezzolani et al. IEPC2017 (Trezzolani et al. 2017b)	0.07	0.85	867	12.1	5.2	Xe
18-Takahashi et al. Fig. 22 (Takahashi and Ando 2018)	6	67	3256	11.2	17.8	Ar

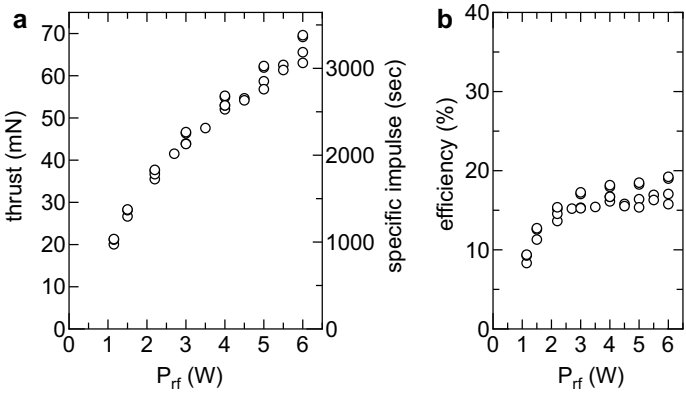

Fig. 22 Recently measured thrust and the simply calculated specific impulse and thruster efficiency from the mass flow rate of the propellant and the rf generator power. The thruster assessed here has the 95-mm-inner-diameter source tube and the gas injection near the thruster exit (Takahashi and Ando 2018)

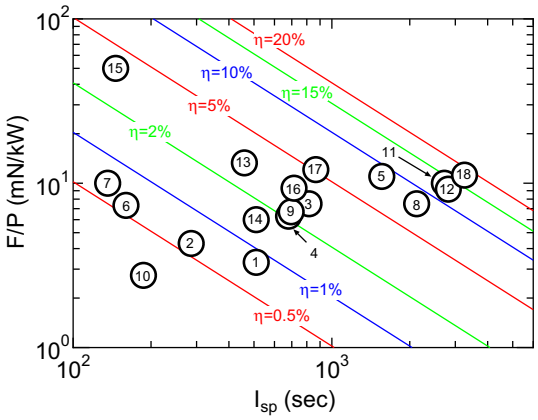

Fig. 23 Thruster performances from Table 1. Equation (37) calculated for various values of the thruster efficiency η are drawn by solid lines, and the numbers in the open circles show the indexes labeled in Table 1

A new application of the helicon plasma thruster to space debris removal is also discussed.

6.1 Helicon thruster assessment

Over the past several years, several research groups have performed the thrust assessment of the rf magnetic nozzle plasma thrusters using the thrust balances or using the target techniques as briefly summarized in Table 1. The specific impulse I_{sp}, the thrust-to-power ratio F/P_{rf}, and the thruster efficiency η_{rf} are also calculated from the measured thrust F and the mass flow rate of the propellant, where the rf generator output power P_{rf} is used for the calculation. Although the first two experiments in 2011 showed the very poor thruster efficiency less than a percent, it can be recognized that the thruster performance is gradually improved. Figure 22 shows the

most recently measured thrust F, the specific impulse I_{sp}, and the thruster efficiency η_{rf} calculated using the rf power P_{rf} from the generator, where the 95-mm-diameter source tube and the gas injection near the open source exit are employed (Takahashi and Ando 2018). It should be mentioned that the data in Fig. 22a present both the thrust and the specific impulse, since the specific impulse is proportional to the thrust for the constant mass flow rate of the propellant. The result clearly shows the best performance to this date and the thruster efficiency is now approaching ~ 20%. Eqs. (1) and (2) give the relation of the thruster efficiency η_{rf}, the specific impulse I_{sp}, and the thrust-to-power ratio F/P_{rf} as

$$\frac{F}{P_{rf}} = \frac{2}{g}\frac{1}{I_{sp}}\eta_{rf}. \tag{37}$$

The relations for various values of η_{rf} are plotted by solid lines in Fig. 23, together with the data obtained from Table 1, where the numbers in the open circle plots show the indexes labeled in the publications of Table 1. Most of the thrusters are characterized as $F/P_{rf} \sim 10$ mN/kW at this moment and the thruster efficiency above 10% was obtained in several experiments, while the specific impulse ranges from 100 to 3000 s due to the wide range of the operating power and the mass flow rate of the propellant. Further optimization and the inhibition of the energy loss will be required to improve the performance further. In author's consideration, the higher performance of plots 11, 12, and 18 in Fig. 23 is obtained by increasing the source size and the magnetic field strength, both of which contribute to inhibit the plasma losses to the wall and from the magnetic nozzle.

6.2 Magnetic nozzle formation by permanent magnets

Needless to say, the solenoid coils consume electricity to generate the magnetic fields and require dc power supplies. The magnetic field has two significant roles in the thruster as described already: the efficient plasma production (by inhibiting the loss and by generating the helicon wave) and the momentum conversion in the magnetic nozzle. However the electricity consumed by the solenoid is finally converted into only heat, i.e., the energy loss. Therefore, exchanging the solenoids into permanent magnets (PMs) is very useful to reduce the consumed electricity; further the dc power supply for the solenoid can be eliminated from the system, resulting in more compact design of the thruster. Here a few types of the PM configurations tested in the helicon source and the thruster are described.

The uses of the PMs in the helicon sources were carried out around 2000 by Hong et al. (2000) and by Sasaki et al. (2001) for plasma-processing reactors, where the cusp magnetic fields corresponding to a null axial magnetic field were formed inside or near the source exit. For the application to the magnetic nozzle plasma thrusters requiring the high plasma density downstream of the source, the presence of the cusp in the source will prevent the plasma from being exhausted from the source. Virko et al. employed the combination of the cylindrical array of the PM bars and the annular PMs to the helicon source and adjusted the position of the cusp (Virko et al. 2010). Chen and Torreblanca used the expanding magnetic field formed

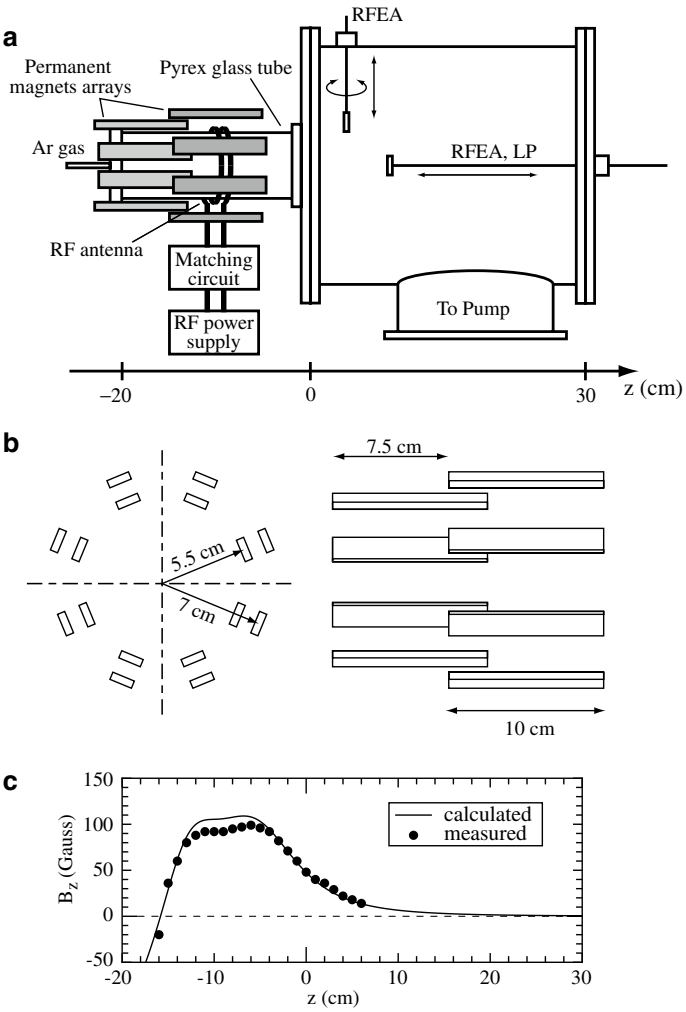

Fig. 24 Schematic of the permanent magnet helicon source experiment containing the CFDL and accelerated ion beam. Figure is taken from Takahashi et al. (2008)

downstream of the annular PMs for the helicon source. The configuration does not contain the cusp both inside and downstream of the source and they utilized the low-field density jump phenomenon (Chen and Torreblanca 2007). Takahashi et al. successfully designed the double-concentric PM arrays forming a constant magnetic field inside the source and a divergent field downstream of the source as shown in Fig. 24 (Takahashi et al. 2008, 2010). Some of the configurations allow the spontaneous generation of the supersonic ion beam generated by a rapid potential drop of the CFDL and contributes to the first direct measurement of the helicon thruster (Takahashi et al. 2011a). Tonooka et al. copied the Takahashis' PM configuration (Tonooka et al. 2015) and re-measure the thrust as well as (Takahashi et al. 2008,

2010, 2011a). Oshio et al. used a annular PM and remains the cusp magnetic field inside the source; the antenna location was surveyed to improve the thruster performance (Oshio et al. 2017).

The maximum magnetic field strength in the PM helicon source tested previously was about 500 Gauss for Virko's configuration (Virko et al. 2010), about 120 Gauss for Chen's configuration (Chen and Torreblanca 2007), and 275 Gauss for Takahashi's configuration (Takahashi et al. 2010, 2013b). Since the thrust imparted by the magnetic nozzle increases with the increase in the magnetic field strength due to the inhibition of the cross-field diffusion (Takahashi et al. 2013a), optimization of the PM configuration providing stronger magnetic field is also one of the engineering challenges.

6.3 rf system

The rf systems mounted on electric propulsion devices have similar problems on their size and weight as well as the solenoids; several types of rf generators and impedance matching techniques have been developed.

The output impedance of the typical generators is designed so as to be 50 Ω; the characteristic impedance of the transmission line and the impedance of the load including the antenna and the plasmas have to be matched to be 50 Ω. Therefore, two variable capacitors are generally mounted on the matching circuit and their capacitances can be tuned by mechanical motion. Reduction of the size of the matching circuit and elimination of the mechanically controlled structure are very useful for the electric propulsion. Charles et al. used the frequency variable power generator operated at around 13.56 ± 0.678 MHz with the fixed small ceramic capacitors, where the impedance tuning was performed by adjusting the frequency (Charles et al. 2013). Takahashi et al. used similar technique for the industrial and electric propulsion applications with the broader-band rf amplifier, which makes the design of the matching circuit easier and successfully observed the transition from the low- to high-density discharge modes (Takahashi et al. 2017). These experiments are performed with a well-established class-AB amplifier.

Compared with the linear amplifier classified as class-A or -AB, switching amplifier of class-D or class-E are known to yield high dc–rf conversion efficiency above 90%. It should be mentioned that the class-D amplifier is operational in the wide range of the frequency less than typically 1 MHz because of the switching loss of the transistors, while the class-E amplifier operational at higher range of the frequency is operational in a narrow range of the frequency than that of the class-D amplifier to realize the zero voltage switching under a LC resonance condition. These were tested in several helicon source and capacitive thruster experiments, where the driving frequency ranges from a few hundreds of kHz to several tens of MHz (Ziemba et al. 2006; Ando et al. 2010; Biggs et al. 2015; Liang et al. 2018). The switched rf power can be transferred to the load via a LC resonance circuit and the power would be controlled by the primary dc voltage.

When mounting these rf amplifiers to the propulsion device, it would be useful to include the auto-matching controller on the system. Furthermore, the net power is

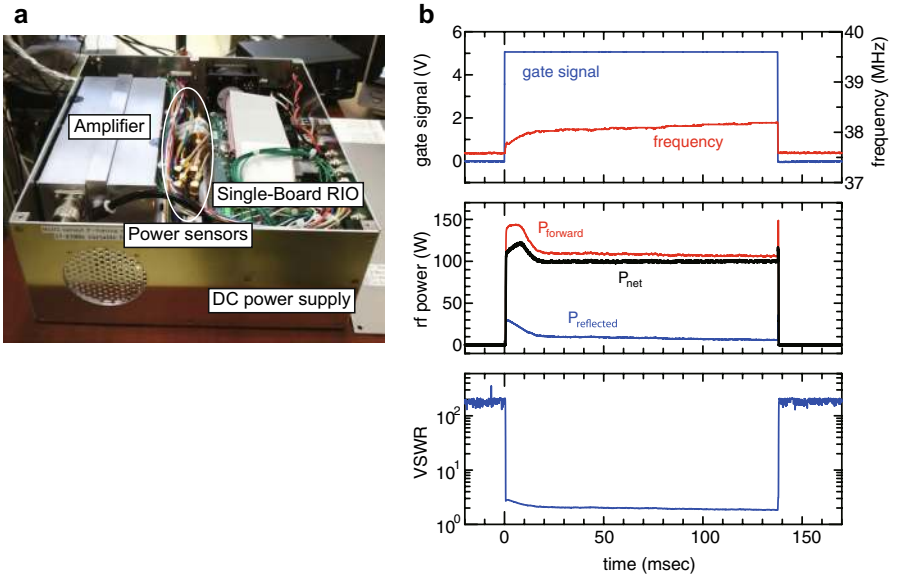

Fig. 25 **a** Photograph of the prototype the rf amplifier including the Single-Board RIO controller. **b** Typical temporal signals of the gate signal, the frequency, the rf powers (P_{forward}, $P_{\text{reflected}}$), the net rf power P_{net}, and the VSWR

favorable to be maintained at constant, rather than maintaining the constant forward power. This technical issue is also under development by the author using an on-board system for both the industrial and space applications, where the class-AB amplifier with 75% dc–rf conversion efficiency and a broad frequency range of 40 ± 3 MHz is used to make the impedance tuning easier. The frequency and the output power can be controlled by adjusting input voltage signals to the voltage controlled oscillator (VCO) and the voltage variable attenuator (VVA) connected to the amplifier. The output power from the amplifier is transferred to a load consisting of small fixed capacitors, an rf antenna, and a plasma via a dual-directional coupler. The signals from the directional coupler are converted into dc voltages using Schottky barrier diode (SBD) detectors. A Single-Board RIO controller (National Instruments) programmed by Labview is used to control and detect these voltage signals, whereby the VCO and VVA signals are automatically controlled so as to minimize the voltage standing wave ratio (VSWR) and to maintain the constant net rf power, respectively. A photograph of the prototype is shown in Fig. 25a. Figure 25b shows the typical temporal signals of the gate signal turning on the rf power, the frequency, the forward power P_{forward}, the reflected power $P_{\text{reflected}}$, the net power $P_{\text{net}} = P_{\text{forward}} - P_{\text{reflected}}$, and the VSWR, where the rf power with the pulse width of ~140 ms is turned on at $t = 0$ ms. It is found that the reflected power and the VSWR are minimized within about 10 ms and the net power is maintained at constant after $t > 20$ ms (Takahashi and Ando 2018). The tuning time will be reduced to optimize the controller program in near future. By integrating the controller into the rf amplifier, the control of the propulsion device operated in space will become easier.

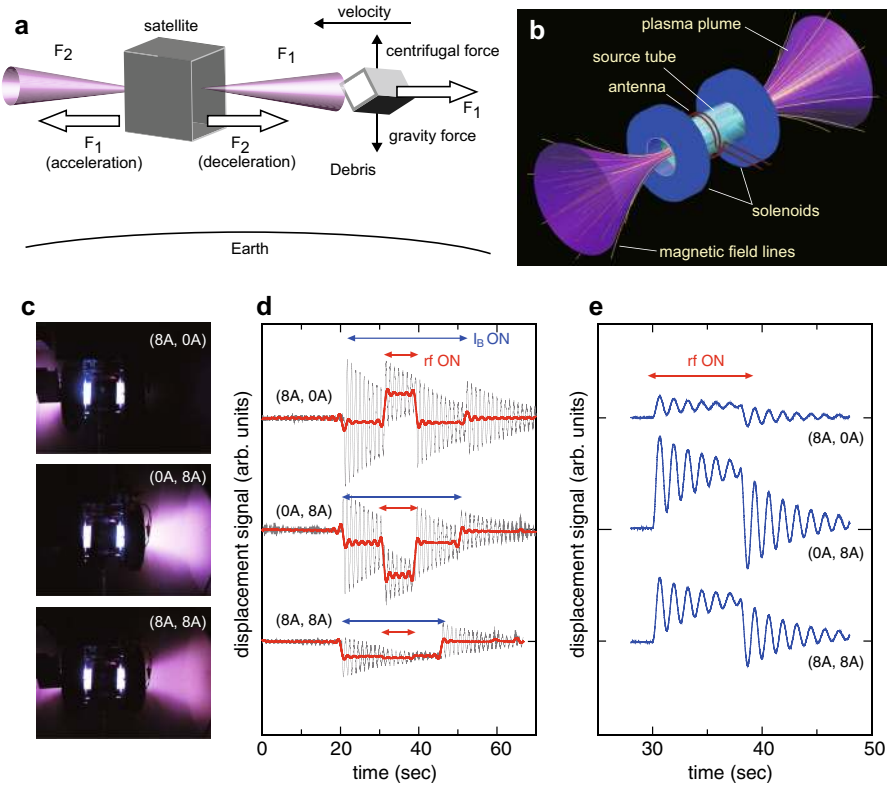

Fig. 26 **a** Concept for space debris removal by bi-directional momentum ejection from a satellite. **b** Schematic of a magnetic nozzle rf plasma thruster having two open source exits. **c** Photographs taken by a digital camera via a vacuum viewport on the chamber side wall for the dc currents of the left and right solenoids (I_{BL}, I_{BR}) = (8 A, 0 A), (0 A, 8 A), and (8 A, 8 A). **d** The raw (gray thin lines) and filtered (red bold lines) displacement signals of the thruster attached to the thrust balance. **e** The displacement signals of the target plate. The positive and negative displacements in **d** and **e** correspond to the rightward and leftward directions, respectively. Figure is taken from Takahashi et al. (2018)

As described above, some rf systems operated in the wide ranges of the frequency and the power have been under development for the application to the rf space propulsion and the industrial plasma devices. Further studies including both the physics described in this paper and the engineering issues will be required.

6.4 Space debris removal by the helicon thruster

Finally, the recently proposed application of the helicon plasma thruster to the active and contactless space debris removal is very briefly described here.

Space debris removal from Earth orbit using a satellite has been an emergent technological challenge for sustainable human activities in space. To deorbit debris, it is necessary to impart a force to decelerate it; they finally re-enter the Earth atmosphere and naturally burn up. A satellite using an energetic plasma

beam directed to the debris will need to eject another plasma beam in the opposite direction in a controlled manner, to maintain a constant distance between it and the debris during the deorbiting mission as shown in Fig. 26a. This has been proposed with two ion-gridded thrusters directed in the opposite directions (Bombardelli and Peláez 2011) and called an ion beam shepherd method. By employing a magnetic nozzle plasma thruster having two open source exits, bi-directional plasma ejection can be achieved using the single electric propulsion device as seen in Fig. 26b and was recently demonstrated in a laboratory experiment (Takahashi et al. 2018). In the experiment, both the forces exerted on the thruster and the target plate simulating the debris are simultaneously measured in a laboratory space simulation chamber showing that a force decelerating the debris and a zero net force on the thruster can be successfully obtained. These two forces to the thruster and the target can be individually controlled by external electrical parameters, resulting in the ability to switch the acceleration and deceleration modes of the satellite and the debris removal mode using a single electric propulsion device. Photographs of these three operation modes and the raw signals of the displacement sensors measuring the thruster and the target are shown in Fig. 26c–e, respectively. For the debris removal mode (bottom of Fig. 26c–e), the zero displacement of the thruster and the finite force to the target can be clearly observed. Therefore, this method will provide the space debris removal using the single electric propulsion device. The required thruster performance for the ion beam shepherd method was analyzed by Bombardelli and Peláez (2011), and the applicable performance of the helicon thruster was also discussed in Takahashi et al. (2018). Further development and mission analysis considering the helicon thruster performance will be required, which is also related with all the topics described in the review, e.g., the thruster performance, the thrust components, the divergence of the accelerated ions and/or the plasma flow, the plasma detachment from the magnetic nozzle, and so on.

7 Summary

The recent studies on the radiofrequency (rf) magnetic nozzle plasma thrusters have been reviewed. Since the rf plasma production inevitably yields the zero global current, i.e., the condition of the ‘current free‘, the thruster can be operated with no neutralizer. Understanding the thrust generation mechanisms in the helicon-type magnetic nozzle plasma thruster has been progressed over the past decade by effort on the theoretical, experimental, and numerical studies, where combining the plasma and thruster diagnostics has significantly contributed via compensating for shortcomings of each other in the laboratory experiments. However, some aspects of physics are not fully understood yet and may include very interesting phenomena, such as the plasma momentum lost to the wall, plasma transport and structural formation in the magnetic nozzle, the detailed momentum conversion processes, and so on. Although the steady-state physics have been mainly discussed for the past decade, the dynamic and temporally varying phenomena also include many aspects of physics, such as plasma instabilities and the resultant plasma transport phenomena.

The plasma detachment from the magnetic nozzle and the electron thermodynamics in the magnetic nozzle are still open questions. The most important issue is the improvement of the performance of the thruster. Furthermore, the technical issues on the peripheral devices such as the rf system and the permanent magnet configurations are also challenging topics. The author thinks that the insights in the thruster studies may also shed light on astrophysics and space physics, and will provide a new technology for the space debris removal.

Compliance with ethical standards

Conflict of interest The author states that there is no conflict of interest.

References

A. Aanesland, C. Charles, M.A. Lieberman, R.W. Boswell, Upstream ionization instability assocated with a current-free double layer. Phys. Rev. Lett. **97**(7), 075003-1–4 (2006)

A. Aanesland, L. Liard, G. Leray, J. Jolly, P. Chabert, Direct measurements of neutral density depletion by two-photon absorption laserinduced fluorescence spectroscopy. Appl. Phys. Lett. **91**(12), 121502-1–3 (2007)

E. Ahedo, M. Merino, Two-dimensional supersonic plasma acceleration in a magnetic nozzle. Phys. Plasmas **17**(7), 073501-1–15 (2010)

E. Ahedo, M. Merino, On plasma detachment in propulsive magnetic nozzles. Phys. Plasmas **18**(5), 053504-1–8 (2011)

E. Ahedo, J. Navarro-Cavallé, Helicon thruster plasma modeling: two-dimensional fluid-dynamics and propulsive performances. Phys. Plasmas **20**(4), 043512-1–13 (2013)

E. Ahedo, M.M. Sánchez, Theory of a stationary current-free double layer in a collisionless plasma. Phys. Rev. Lett. **103**(13), 135002-1–4 (2009)

H. Amemiya, Sheath formation criterion and ion flux for non-Maxwellian plasma. J. Phys. Soc. Jpn. **66**(5), 1335–1338 (1997)

A. Ando, T. Watanabe, T. Watanabe, H. Tobari, K. Hattori, M. Inutake, Evaluation of para-perp type Mach probe by using a fast flowing plasma. J. Plasma Fusion Res. **81**(6), 451–457 (2005)

A. Ando, A. Komuro, T. Matsuno, K. Tsumori, Y. Takeiri, Radio frequency ion source operated with field effect transistor based radio frequency system. Rev. Sci. Instrum. **81**(2), 02B107-1–3 (2010)

A.V. Arefiev, B.N. Breizman, Magnetohydrodynamic scenario of plasma detachment in a magnetic nozzle. Phys. Plasmas **12**(4), 043504-1–10 (2005)

A.V. Arefiev, B.N. Breizman, Ambipolar acceleration of ions in a magnetic nozzle. Phys. Plasmas **15**(4), 042109-1–8 (2008)

O.V. Batishchev, Minihelicon plasma thruster. IEEE Trans. Plasma Sci. **37**(8), 1563–1571 (2009)

D.F. Berisford, R.D. Bengtson, L.L. Raja, Power balance and wall erosion measurements in a helicon plasma. Phys. Plasmas **17**(3), 033503-1–11 (2010)

D. Biggs, S. Avery, L. Raymond, W. Liang, N. Gascon, A.L. Fabris, J. Rivas-Davila, M. Cappelli, A compact helicon thruster for CubeSat applications. Presented at joint conference of 30th international symposium on space technology and science, 34th international electric propulsion conference, and 6th nano-satellite symposium, Hyogo-Kobe, Japan. IEPC – 2015 – 244^{I}*STS* – 2015 – *b* – 244 (2015)

C. Biloiu, X. Sun, E. Choueiri, F. Doss, E. Scime, J. Heard, R. Spektor, D. Ventura, Evolution of the parallel and perpendicular ion velocity distribution functions in pulsed helicon plasma sources obtained by time resolved laser induced fluorescence. Plasma Sources Sci. Technol. **14**(4), 766–776 (2005)
I.A. Biloiu, E.E. Scime, C. Biloiu, Ion beam acceleration in a divergent magnetic field. Appl. Phys. Lett. **92**(19), 191502-1–3 (2008)
C. Bombardelli, J. Peláez, Ion beam shepherd for contactless space debris removal. J. Guid. Control. Dyn. **34**(3), 916–920 (2011)
R.W. Boswell, Plasma production using a standing helicon wave. Phys. Lett. **33A**(7), 457–458 (1970)
R.W. Boswell, F.F. Chen, Helicons—the early years. IEEE Trans. Plasma Sci. **25**(6), 1229–1244 (1997)
R. Boswell, C. Charles, P. Alexander, J. Dedrick, K. Takahashi, Plasma expansion from a radio frequency microdischarge. IEEE Trans. Plasma Sci. **39**(11), 2512–2513 (2011)
R.W. Boswell, K. Takahashi, C. Charles, I.D. Kaganovich, Non-local electron energy probability function in a plasma expanding along a magnetic nozzle. Front. Phys. **3**, 14-1–5 (2015)
B.N. Breizman, M.R. Tushentsov, A.V. Arefiev, Magnetic nozzle and plasma detachment model for a steady-state flow. Phys. Plasmas **15**(5), 057103-1–10 (2008)
J.R. Brophy, NASA's Deep Space 1 ion engine (plenary). Rev. Sci. Instrum. **73**(2), 1071–1078 (2002)
F. Cannat, T. Lafleur, J. Jarrige, P. Chabert, P.-Q. Elias, D. Packan, Optimization of a coaxial electron cyclotron resonance plasma thruster with an analytical model. Phys. Plasmas **22**(5), 053503-1–11 (2015)
F.R. Chang-Diaz, The VASIMR Rocket. Sci. Am. **283**(5), 90–97 (2000)
C. Charles, Spatially resolved energy analyzer measurements of an ion beam on the low potential side of a curret-free double-layer. IEEE Trans. Plasma Sci. **33**(2), 336–337 (2005)
C. Charles, A review of recent laboratory double layer experiments. Plasma Sources Sci. Technol. **16**(4), R1–R25 (2007). **(references therein)**
C. Charles, Plasmas for spacecraft propulsion. J. Phys. D: Appl. Phys. **42**(16), 163001-1–18 (2009)
C. Charles, High density conics in a magnetically expanding helicon plasma. Appl. Phys. Lett. **96**(5), 051502-1–3 (2010)
C. Charles, R.W. Boswell, Current-free double-layer formation in a high-density helicon discharge. Appl. Phys. Lett. **82**(9), 1356–1358 (2003)
C. Charles, R.W. Boswell, Laboratory evidence of a supersonic ion beam generated by a current-free "helicon" double-layer. Phys. Plasmas **11**(4), 1706–1714 (2004)
C. Charles, R.W. Boswell, The magnetic-field-induced transition from an expanding plasma to a double layer containing expanding plasma. Appl. Phys. Lett. **91**(20), 201505-1–3 (2007)
C. Charles, R.W. Boswell, A. Bouchoule, C. Laure, P. Ranson, Plasma diffusion from a low pressure radio frequency source. J. Vac. Sci. Technol. A **9**(3), 661–663 (1991)
C. Charles, R.W. Boswell, R. Lane, P. MacLellan, An experimental investigation of alternative propellants for the helicon double layer thruster. J. Phys. D: Appl. Phys. **41**(17), 175213-1–6 (2008)
C. Charles, R. Boswell, P. Alexander, C. Costa, O. Surtherland, L. Pfitzner, R. Franzen, J. Kingwell, A. Parfitt, P.-E. Frigot, J.D. Amo, G. Saccoccia, I.E.E.E. Trans, Plasma Sci. **36**(4), 1196–1197 (2008)
C. Charles, R.W. Boswell, R. Hawkins, Oblique double layers: a comparison between terrestrial and auroral measurements. Phys. Rev. Lett. **103**(9), 095001-1–4 (2009)
C. Charles, K. Takahashi, R.W. Boswell, Axial force imparted by a conical radiofrequency magnetoplasma thruster. Appl. Phys. Lett. **100**(11), 113504-1–3 (2012)
C. Charles, R. Boswell, K. Takahashi, Boltzmann expansion in a radiofrequency conical helicon thruster operating in xenon and argon. Appl. Phys. Lett. **102**(22), 223510-1–4 (2013)
C. Charles, R.W. Boswell, A. Bish, Variable frequency matching to a radiofrequency source immersed in vacuum. J. Phys. D: Appl. Phys. **46**(36), 365203-1–6 (2013)
C. Charles, R.W. Boswell, A. Bish, Low-weight fixed ceramic capacitor impedance matching system for an electrothermal plasma microthruster. J. Propul. Power **30**(4), 1117–1121 (2014)
D.G. Chavers, F.R. Chang-Diaz, Momentum flux measuring instrument for neutral and charged particle flow. Rev. Sci. Instrum. **73**(10), 3500–3507 (2002)
F.F. Chen, The low-field density peak in helicon discharges. Phys. Plasmas **10**(6), 2586–2592 (2003)
F.F. Chen, Physical mechanism of a current-free double layer. Phys. Plasmas **13**(3), 034502-1–3 (2006)
F.F. Chen, R.W. Boswell, Helicons—the past decade. IEEE Trans. Plasma Sci. **25**(6), 1245–1257 (1997)
R.T.S. Chen, N. Hershkowitz, Multiple electron beams generated by a helico plasma discharges. Phs. Rev. Lett. **80**(21), 4677–4680 (1998)

F.F. Chen, H. Torreblanca, Large-area helicon plasma source with permanent magnets. Plasma Phys. Control. Fusion **49**(5A), A81–A93 (2007)
K. Chung, Mach probes. Plasma Sources Sci. Technol. **21**(6), 063001-1–47 (2012)
S.A. Cohen, N.S. Siefert, S. Stange, R.F. Boivin, E.E. Scime, F.M. Levinton, Ion acceleration in plasmas emerging from a helicon-heated magnetic-mirror device. Phys. Plasmas **10**(6), 2593–2598 (2003)
S.A. Cohen, X. Sun, N.M. Ferraro, E.E. Scime, M. Miah, S. Stange, N.S. Siefert, R.F. Boivin, I.E.E.E. Trans, Plasma Sci. **34**(3), 792–803 (2006)
C.S. Corr, R.W. Boswell, High-beta plasma effects in a low-pressure helicon plasma. Phys. Plasmas **14**(12), 122503-1–7 (2007)
C.S. Corr, R.W. Boswell, C. Charles, J. Zanger, Spatial evolution of an ion beam created by a geometrically expanding low-pressure argon plasma. Appl. Phys. Lett. **92**(22), 221508-1–3 (2008)
W. Cox, C. Charles, R.W. Boswell, R. Hawkins, Spatial retarding field energy analyzer measurements downstream of a helicon double layer plasma. Appl. Phys. Lett. **93**(7), 071505-1–3 (2008)
W. Cox, R. Hawkins, C. Charles, R. Boswell, Three-dimensional mapping of ion density in a double-layer helicon plasma. IEEE Trans. Plasma Sci. **36**(4), 1386–1387 (2008)
P.A. Davidson, *An Introduction to Magnetohydrodynamics*, Chap. 2 (Cambridge University Press, Cambridge, 2001)
A.W. Degeling, C.O. Jung, R.W. Boswell, A.R. Ellingboe, Plasma production from helicon waves. Phys. Plasmas **3**(7), 2788–2796 (1996)
A.W. Degeling, T.E. Sheridan, R.W. Boswell, Intense on-axis plasma production and associated relaxation oscillations in a large volume helicon source. Phys. Plasmas **6**(9), 3664–3673 (1999)
C.A. Deline, R.D. Bengtson, B.N. Breizman, M.R. Tushentsov, J.E. Jones, D.G. Chavers, C.C. Dobson, B.M. Schuettpelz, Plume detachment from a magnetic nozzle. Phys. Plasmas **16**(3), 033502-1–9 (2009)
C.M. Denning, M. Wiebold, J.E. Scharer, Observations of neutral depletion and plasma acceleration in a flowing high-power argon helicon plasma. Phys. Plasmas **15**(7), 072115-1–12 (2008)
K.D. Diamant, J.E. Pollard, R.B. Cohen, Y. Raitses, N.J. Fisch, Segmented electrode Hall thruster. J. Propul. Power **22**(6), 1396–1401 (2006)
T.V. Doorsselaere, N. Wardle, G.D. Zanna, K. Jansari, E. Verwichte, V.M. Nakariakov, The first measurement of the adiabatic index in the solar corona using time-dependent spectroscopy of HINODE/EIS observations. Astrophys. J. Lett. **727**(2), L32-1–4 (2011)
C.M. Franck, O. Grulke, T. Klinger, Transition from unbounded to bounded plasma whistler wave dispersion. Phys. Plasmas **9**(8), 3254–3258 (2002)
C.M. Franck, O. Grulke, T. Klinger, Mode transitions in helicon dischargs. Phys. Plasmas **10**(1), 323–325 (2003)
A. Fruchtman, Electric field in a double layer and the imparted momentum. Phys. Rev. Lett. **96**(6), 065002-1–4 (2006)
A. Fruchtman, Neutral depletion in a collisionless plasma. IEEE Trans. Plasma Sci. **36**(2), 403–413 (2008a)
A. Fruchtman, Energizing and depletion of neutrals by a collisional plasma. Plasma Sources Sci. Technol. **17**(2), 024016-110 (2008b)
A. Fruchtman, Ambipolar and nonambipolar cross-field diffusions. Plasma Sources Sci. Technol. **18**(2), 025033-1–16 (2009)
A. Fruchtman, Nonmonotonic plasma density profile due to neutral-gas depletion. Phys. Plasmas **17**(2), 023502-1–8 (2010)
A. Fruchtman, The thrust of a collisional-plasma source. IEEE Trans. Plasma Sci. **39**(1), 530–539 (2011)
A. Fruchtman, Enhanced thrust due to ion-neutral collisions for electric propulsion. Plasma Chem. Plasma Process. **34**(3), 647–660 (2014)
A. Fruchtman, Neutral gas depletion in low temperature plasma. J. Phys. D: Appl. Phys. **50**, 473002-1–31 (2017)
A. Fruchtman, G. Makrinich, P. Chabert, J.M. Rax, Enhanced plasma transport due to neutral depletion. Phys. Rev. Lett. **95**, 115002-1–4 (2005)
A. Fruchtman, G. Makrinich, J.-L. Raimbault, L. Liard, J.-M. Rax, P. Chabert, Neutral depletion versus repletion due to ionization. Phys. Plasmas **15**(5), 057102-1–7 (2008)
A. Fruchtman, K. Takahashi, C. Charles, R.W. Boswell, A magnetic nozzle calculation of the force on a plasma. Phys. Plasmas **19**(3), 033507-1–6 (2012)
F. Gesto, C. Charles, R. Boswell, Xenon ion beam detachment from a helicon double layer thruster. IEEE Trans. Plasma Sci. **36**(4), 1194–1195 (2008)

S. Ghosh, S. Yadav, K.K. Barada, P.K. Chattopadhyay, J. Ghosh, R. Pal, D. Bora, Formation of annular plasma downstream by magnetic aperture in the helicon experimental device. Phys. Plasmas **24**(2), 020703-1–6 (2017)
S. Giannelli, A. Kieckhafer, M.L.R. Walker, Neutral gas expansion in a cylindrical helicon discharge chamber. J. Propul. Power **29**(3), 540–546 (2013)
V.A. Godyak, R.B. Piejak, B.M. Alexandrovich, The electron-energy distribution function in a shielded argon radiofrequency inductive discharge. Plasma Sources Sci. Technol. **4**, 332–336 (1995)
V.A. Godyak, R.B. Piejak, B.M. Alexandrovich, Electron energy distribution function measurements and plasma parameters in inductively coupled argon plasma. Plasma Sources Sci. Technol. **11**, 525–543 (2002)
D.M. Goebel, I. Katz, *Fundamentals of Electric Propulsion: Ion and Hall Thrusters* (Wiley, Hoboken, 2008)
J.T. Gudmundsson, On the effect of the electron energy distribution on the plasma parameters of an argon discharge: a global (volume-averaged) model study. Plasma Sources Sci. Technol. **10**(1), 76–81 (2001)
T. Harle, S.J. Pottinger, V.J. Lappas, Helicon double layer thruster operation in a low magnetic field mode. Plasma Sources Sci. Technol. **22**(1), 015015-1–7 (2013)
N. Hershkowitz, Review of recent laboratory double layer experiments. Space Sci. Rev. **41**, 351–391 (1985)
M.J. Hole, S.W. Simpson, Performance of a vacuum arc centrifuge with a nonuniform magnetic field. Phys. Plasmas **4**(10), 3493–3500 (1997)
I.S. Hong, Y.S. Hwang, G.H. Lee, D.Y. Kim, H.Y. Won, G.S. Eom, W. Choe, Ion-beam characteristics of novel helicon ion sources for different plasma parameters. Rev. Sci. Instrum. **71**(3), 1385–1388 (2000)
E.B. Hooper, Plasma detachment from a magnetic nozzle. J. Propul. Power **9**(5), 757–763 (1993)
J. Hoopwood, Review of inductively coupled plasmas for plasma processing. Plasma Sources Sci. Technol. **1**, 109–116 (1992)
I.H. Hutchinson, *Principles of Plasma Diagnoses, Chap. 3*, 2nd edn. (Cambridge University Press, Cambridge, 2002)
Y. Igarashi, K. Takahashi, T. Fujiwara, Energetic electrons moving along peripheral magnetic field lines in magnetically expanding plasmas. IEEE Trans. Plasma Sci. **39**(11), 2442–2443 (2011)
C. Jacobs, S. Poedts, A polytropic model for the solar wind. Adv. Space Res. **48**, 1958–1966 (2011)
R.G. Jahn, *Physics of Electric Propulsion* (Dover, New York, 2006), p. 138
H. Kang, D. Kim, M. Lee, C. Chung, Improved numerical AC superposition method for electron energy distribution functions. Phys. Plasmas **24**(11), 113509-1–4 (2017)
Y. Kato, S. Mineshige, K. Shibata, Magnetohydrodynamic accetion flows: formation of magnetic tower jet and subsequent quasi-steady state. Astrophy. J. **605**, 307–320 (2004)
A.M. Keesee, E.E. Scime, Neutral argon density profile determination by comparison of spectroscopic measurements and a collisional-radiative model (invited). Rev. Sci. Instrum. **77**(10), 10F304-1–6 (2006)
A.M. Keesee, E.E. Scime, Neutral density profiles in argon helicon plasmas. Plasma Sources Sci. Technol. **16**(4), 742–749 (2007)
J.Y. Kim, K.S. Chung, S. Kim, J.H. Ryu, K.-J. Chung, Y.S. Hwang, Thermodynamics of a magnetically expanding plasma with isothermally behaving confined electrons. New J. Phys. **20**, 063033-1–11 (2018)
C.R. Koppel, F. Marchandise, M. Prioul, D. Estublier, F. Darnon, The SMART-1 electric propulsion subsystem around the moon: in flight experience, 41st AIAA/ASME/SAE/ASEE joint propulsion conference and exhibit, Tucson, USA. AIAA **2005–3671** (2005)
U. Kortshagen, H. Schlüter, Determination of electron energy distribution functions in surface wave produced plasmas: II. measurements. J. Phys. D: Appl. Phys. **24**, 1585–1593 (1991)
U. Kortshagen, I. Pukropski, M. Zethoff, Spatial variation of the electron distribution function in a rf inductively coupled plasma: experimental and theoretical study. J. Appl. Phys. **76**(4), 2048–2058 (1994)
H. Kuninaka, K. Nishiyama, I. Funaki, Y. Shimizu, T. Yamada, J. Kawaguchi, Assessment of plasma interactions and flight status of the HAYABUSA asteroid explorer propelled by microwave discharge ion engines. IEEE Trans. Plasma Sci. **34**(5), 2125–2132 (2006)
K. Kuriki, M. Inutake, Super-Alfvenic flow and collision free shock wave in a plasma wind tunnel. Phys. Fluids **17**(1), 92–99 (1974)

D. Kuwahara, S. Shinohara, K. Yano, Thrust characteristics of high-density helicon plasma using argon and xenon gases. J. Propul. Power **33**(2), 420–424 (2017)
T. Lafleur, Helicon plasma thruster discharge model. Phys. Plasmas **21**(4), 043507-1–11 (2014)
T. Lafleur, K. Takahashi, C. Charles, R.W. Boswell, Direct thrust measurements and modelling of a radio-frequency expanding plasma thruster. Phys. Plasmas **18**(8), 080701-1–4 (2011)
T. Lafleur, F. Cannat, J. Jarrige, P.Q. Elias, D. Packan, Electron dynamics and ion acceleration in expanding-plasma thrusters. Plasma Sources Sci. Technol. **24**(6), 065013-1–13 (2015)
D. Lee, N. Hershkowitz, Ion collection by planar Langmuir probes: Sheridan's model and its verification. Phys. Plasmas **14**(3), 033507-1–4 (2007)
W. Liang, C. Charles, L. Raymond, A. Stuchbery, K. Surakitbovorn, L. Gu, R. Boswell, J. Rivas-Davila, An integrated RF power delivery and plasma micro-thruster system for nano-satellites. Front. Phys. **6**, 115-1–9 (2018)
L. Liard, J.-L. Raimbault, J.-M. Rax, P. Chabert, Plasma transport under neutral gas depletion conditions. J. Phys. D: Appl. Phys. **40**(17), 5192–5195 (2007)
M.A. Lieberman, C. Charles, Theory for formation of a low-pressure, current-free double layer. Phys. Rev. Lett. **97**(4), 045003-1–4 (2006)
M.A. Lieberman, A.J. Lichtenberg, *Principles of Plasma Discharges and Materials Processing*, 2nd edn. (Wiley, Hoboken, 2005)
J. Ling, M.D. West, T. Lafleur, C. Charles, R.W. Boswell, Thrust measurements in a low-magnetic field high-density mode in the helicon double layer thruster. J. Phys. D: Appl. Phys. **43**(30), 305203-1–9 (2010)
J. Ling, R.W. Boswell, T. Lafleur, C. Charles, Microarcing in a helicon plasma reactor. IEEE Trans. Plasma Sci. **39**(8), 1652–1659 (2011)
G. Listano, M. Fontanesi, S. Bernabei, Propagation of electron cyclotron waves along a magnetic beach. Phys. Rev. Lett. **26**(13), 747–750 (1971)
J.M. Little, E.Y. Choueiri, Critical condition for plasma confinement in the source of a magnetic nozzle plasma flow. IEEE Trans. Plasma Sci. **43**(1), 277–286 (2015)
J.M. Little, E.Y. Choueiri, Electron cooling in a magnetically expanding plasma. Phys. Rev. Lett. **117**(22), 225003-1–5 (2016)
B. Longmier, B.M. Reid, A. Gallimore, F.R. Chang-Diaz, J.P. Squire, T.W. Glover, G. Chavers, E.A. Berring III, Validating a plasma momentum flux sensor to an inverted pendulum thrust stand. J. Propul. Power **25**(3), 746–752 (2009)
B.W. Longmier, E.A. Bering III, M.D. Carter, L.D. Cassady, W.J. Chancery, F.R. Chang Diaz, T.W. Glover, N. Hershkowitz, A.V. Ilin, G.E. McCaskill, C.S. Olsen, J.P. Squire, Plasma Sources Sci. Technol **20**(1), 015007-1–9 (2011)
B.W. Longmier, L.D. Cassady, M.G. Ballenger, M.D. Carter, F.R. Chang-Diaz, T.W. Glover, A.V. Ilin, G.E. McCaskill, C.S. Olsen, J.P. Squire, VX-200 magnetoplasma thruster performance results exceeding fifty-percent thruster efficiency. J. Propul. Power **27**(4), 915–920 (2011)
B.W. Longmier, J.P. Squire, C.S. Olsen, L.D. Cassady, M.G. Ballenger, M.D. Carter, A.V. Ilin, T.W. Glover, G.E. McCaskill, F.R. Chang Díaz, E.A. Bering III, Improved efficiency and throttling range of the VX-200 magnetoplasma thruster. J. Propul. Power **30**(1), 123–132 (2014)
J. Lukas, G. Teel, J. Kolbeck, M. Keidar, High thrust-to-power ratio micro-cathode arc thruster. AIP Adv. **6**(2), 025311-1–7 (2016)
R.M. Magee, M.E. Galante, J. Carr Jr., G. Lusk, D.W. McCarren, E.E. Scime, Neutral depletion and the helicon density limit. Phys. Plasmas **20**(12), 123511-1–5 (2013)
G. Makrinich, A. Fruchtman, Enhancement of electric force by ion-neutral collisions. Appl. Phys. Lett. **95**(18), 181504-1–3 (2009)
W.M. Manheimer, R.F. Fernsler, Plasma acceleration by area expansion. IEEE Trans. Plasma Sci. **29**(1), 75–84 (2001)
K. Martinez-Sanchez, I.E. Pollard, Spacecraft electric propulsion—an overview. J. Propul. Power. **14**(5), 688–699 (1998)
A. Meige, R.W. Boswell, Electron energy distribution functions in low-pressure inductively coupled bounded plasmas. Phys. Plasmas **13**(9), 092104-1–5 (2006)
A. Meige, R.W. Boswell, C. Charles, J.-P. Boeuf, G. Hagellar, M.M. Turner, One-dimensional simulation of an ion beam generated by a current-free double-layer. IEEE Trans. Plasma Sci. **33**(2), 334–335 (2005)
M. Merino, E. Ahedo, Plasma detachment in a propulsive magnetic nozzle via ion demagnetization. Plasma Sources Sci. Technol. **23**(3), 032001-1–5 (2014)

M. Merino, E. Ahedo, Effect of the plasma-induced magnetic field on a magnetic nozzle. Plasma Sources Sci. Technol. **25**(4), 045012-1–9 (2016)
M. Merino, E. Ahedo, Fully magnetized plasma flow in a magnetic nozzle. Phys. Plasmas **23**(2), 023506-1–7 (2016)
Z. Mikic, D.C. Barnes, D.D. Schnack, Dynamical evolution of a solar coronal magnetic field arcade. Astrophys. J. **328**, 830–847 (1988)
T. Motomura, S. Shinohara, T. Tanikawa, K.P. Shamrai, Characteristics of low-aspect ratio, large-diameter, high-density helicon plasmas with variable axial boundary conditions. Phys. Plasmas **19**(4), 043504-1–12 (2012)
N. Nagao, S. Yokota, K. Komurasaki, Y. Arakawa, Development of a two-dimensional dual pendulum thrust stand for Hall thrusters. Rev. Sci. Instrum. **78**(11), 115108-1–4 (2007)
K. Nagaoka, A. Okamoto, S. Yoshimura, M.Y. Tanaka, Plasma flow measurement using directional Langmuir probe under weakly ion-magnetized conditions. J. Phys. Soc. Jpn. **70**(1), 131–137 (2001)
D. O'Connell, T. Gans, D.L. Crintea, U. Czarnetzki, N. Sadeghi, Neutral gas depletion mechanisms in dense low-temperature argon plasmas. J. Phys. D: Appl. Phys. **41**(3), 035208-1–7 (2008)
A. Okamoto, K. Hara, K. Nagaoka, S. Yoshimura, J. Vranješ, M. Kono, M.Y. Tanaka, Experimental observation of a tripolar vortex in a plasma. Phys. Plasmas **10**(6), 2211–2216 (2003)
C.S. Olsen, M.G. Ballenger, M.D. Carter, F.R. Chang-Diaz, M. Giambusso, T.W. Glover, A.V. Ilin, J.P. Squire, B.W. Longmier, E.A. Bering III, P.A. Cloutier, Investigation of plasma detachment from a magnetic nozzle in the plume of the VX-200 magnetoplasma thruster. IEEE Trans. Plasma Sci. **43**(1), 252–268 (2015)
Y. Oshio, T. Shimada, H. Nishida, Experimental investigation of thrust performance on position relationship between RF antenna and magnetic cusp of RF plasma thruster. Presented at the 35th international electric propulsion conference, Atlanta, Georgia, USA. IEPC-2017-344 (2017)
E.N. Parker, Dynamics of the interplanetary gas and magnetic fields. Astrophys. J. **128**, 664–676 (1958)
N. Plihon, P. Chabert, C.S. Corr, Experimental investigation of double layers in expanding plasmas. Phys Plasmas **14**(1), 013506 (2007)
S. Pottinger, V. Lappas, C. Charles, R. Boswell, Performance characterization of a helicon double layer thruster using direct thrust measurements. J. Phys. D: Appl. Phys. **44**(23), 235201-1–5 (2011)
J. Prager, R. Winglee, T. Ziemba, B.R. Roberson, G. Quetin, Ion energy characteristics downstream of a high power helicon. Plasma Sources Sci. Technol. **17**(2), 025003-1–12 (2008)
S. Rao, N. Singh, Numerical simulation of current-free double layers created in a helicon plasma device. Phys. Plasmas **19**(9), 093507-1–6 (2012)
A. Retinó, A journey through scales. Nat. Phys. **12**, 1092–1093 (2016)
B.R. Roberson, R. Winglee, J. Prager, Enhanced diamagnetic perturbations and electric currents observed downstream of the high power helicon. Phys. Plasmas **18**(5), 053505-1–11 (2011)
S.K. Saha, S. Chowdhury, M.S. Janaki, A. Ghosh, A.K. Hui, S. Raychaudhuri, Plasma density accumulation on a conical surface for diffusion along a diverging magnetic field. Phys. Plasmas **21**(4), 043502-1–8 (2014)
Y. Sakawa, T. Takino, T. Shoji, Control of antenna coupling in high-density plasma production by $m = 0$ helicon waves. Appl. Phys. Lett. **73**(12), 1643–1645 (1998)
Y. Sakawa, H. Kunimatsu, H. Kikuchi, Y. Fukui, T. Shoji, Plasma production by helicon and slow waves. Phys. Rev. Lett. **90**(10), 105001-1–4 (2003)
K. Sasaki, H. Kokubu, D. Hayashi, K. Kadota, Development of a compact nitrogen radical source by helicon-wave discharge employing a permanent magnet. Thin Solid Films **386**, 243–247 (2001)
A. Sasoh, Simple formulation of magnetoplasmadynamic acceleration. Phys. Plasmas **1**(3), 464–469 (1994)
G. Sato, W. Oohara, R. Hatakeyama, Efficient plasma source providing pronounced density peaks in the range of very low magnetc fields. Appl. Phys. Lett. **85**(18), 4007–4009 (2004)
P.F. Schmit, N.J. Fisch, Magnetic detachment and plume control in escaping magnetized plasma. J. Plasma Phys. **75**(3), 359–371 (2009)
K.F. Schoenberg, Pulsed electrostatic probes as a diagnostic for transient plasmas. Rev. Sci. Instrum. **49**(10), 1377–1383 (1978)
A. Shabshelowitz, A.D. Gallimore, Performance and probe measurements of a radio-frequency plasma thruster. J. Propul. Power **29**(4), 919–929 (2013)
J.P. Sheehan, B.W. Longmier, E.A. Bering, C.S. Olsen, J.P. Squire, M.G. Ballenger, M.D. Carter, L.D. Cassady, F.R. Chang Diaz, T.W. Glover, A.V. Ilin, Temperature gradients due to adiabatic plasma expansion in a magnetic nozzle. Plasma Sources Sci. Technol **23**(4), 045014-1–7 (2014)

T.E. Sheridan, How big is a small Langnuir probe? Phys. Plasmas **7**(7), 3084–3088 (2000)
M. Shimada, G.R. Tynan, R. Cattolica, Neutral gas density depletion due to neutral gas heating and pressure balance in an inductively coupled plasma. Plasma Sources Sci. Technol. **16**(1), 193–199 (2007)
S. Shinohara, T. Motomura, K. Tanaka, T. Tanikawa, K.P. Shamrai, Large-area high-density helicon plasma sources. Plasma Sources Sci. Technol. **19**(3), 034018-1–7 (2010)
S. Shinohara, D. Kuwahara, K. Yano, A. Fruchtman, Suppression of diamagnetism by neutrals pressure in partially ionized, high-beta plasma. Phys. Plasmas **23**(12), 122108-1–7 (2016)
S. Shinohara, D. Kuwahara, T. Furukawa, S. Nishhimura, T. Yamase, Y. Ishigami, H. Horita, A. Igarashi, S. Nishimoto, Development of featured high-density helicon sources and their application to electrodeless plasma thruster. Plasma Phys. Control. Fusion **61**(1), 014017-1–11 (2019)
M.U. Siddiqui, C. Cretel, J. Synowiec, A.G. Hsu, J.A. Young, R. Spektor, First performance measurements of the phase four RF thruster. Presented at The 35th international electric propulsion conference, Atlanta, Georgia, USA. IEPC-2017-431 (2017)
N. Singh, S. Rao, P. Ranganath, Waves generated in the plasma plume of helicon magnetic nozzle. Phys. Plasmas **20**(3), 032111-1–7 (2013)
J.S. Snyder, D.M. Goebel, R.R. Hofer, J.E. Polk, N.C. Wallace, H. Simpson, Performance evaluation of the T6 ion engine. J. Propul. Power **28**(2), 371–379 (2012)
A. Spethmann, T. Trottenberg, H. Kersten, Measurement and simulation of forces generated when a surface is sputtered. Phys. Plasmas **24**(9), 093501-1–8 (2017)
R.L. Stenzel, Whistler wave propagation in a large magnetoplasma. Phys. Fluids **19**(6), 857–864 (1976)
R.L. Stenzel, J.M. Urrutia, Electron magnetohydrodynamic turbulece in a high-beta plasma. I. Plasma parameters and instability conditions. Phys. Plasmas **7**(11), 4450–4456 (2000)
R.L. Stenzel, J.M. Urrutia, Helicons in unbounded plasmas. Phys. Rev. Lett. **114**(20), 205005-1–5 (2015)
T.H. Stix, *The Theory of Plasma Waves* (McGraw-Hill Inc, USA, 1962)
I.D. Sudit, F.F. Chen, RF compensated probes for high-density discharges. Plasma Sources Sci. Technol. **3**, 162–168 (1994)
X. Sun, A.M. Keesee, C. Biloiu, E.E. Scime, A. Meige, C. Charles, R.W. Boswell, Observations of ion-beam formation in a current-free double layer. Phys. Rev. Lett. **95**(2), 025004-1–4 (2005)
O. Sutherland, C. Charles, N. Plihon, R.W. Boswell, Experimental evidence of a double layer in a large volume helicon reactor. Phs. Rev. Lett. **95**(20), 205002-1–4 (2005)
D.G. Swanson, *Plasma Waves*, 2nd edn. (Institute of Physics Publishing, Bristol and Philadelphia, 2003)
K. Takahashi, A. Ando, *private communication* (2018)
K. Takahashi, Radiofrequency antenna for suppression of parasitic discharges in a helicon plasma thruster experiment. Rev. Sci. Instrum. **83**(8), 083508-1–4 (2012)
K. Takahashi, A. Ando, Laboratory observation of a plasma-flow-state transition from diverging to stretching a magnetic nozzle. Phys. Rev. Lett. **118**(22), 225002-1–5 (2017)
K. Takahashi, A. Ando, Enhancement of axial momentum lost to the radial wall by the upstream magnetic field in a helicon source. Plasma Phys. Control. Fusion **59**(5), 054007-1–7 (2017)
K. Takahashi, T. Fujiwara, Observation of weakly and strongly diverging ion beams in a magnetically expanding plasma. Appl. Phys. Lett. **94**(6), 061502-1–3 (2009)
K. Takahashi, T. Fujiwara, Ion energy distributions in a permanent-magnet-expanded plasma containing an electric double layer. IEEE Trans. Plasma Sci. **39**(11), 2444–2445 (2011)
K. Takahashi, T. Kaneko, R. Hatakeyama, Polarization-reversal-induced damping of left-hand polarized wave on electron cyclotron resonance. Phys. Rev. Lett. **94**(21), 215001-1–4 (2005a)
K. Takahashi, T. Kaneko, R. Hatakeyama, Effects of polarization reversal on localized-absorption characteristics of electron cyclotron wave in bounded plasmas. Phys. Plasmas **12**(10), 102107-1–7 (2005b)
K. Takahashi, C. Charles, R.W. Boswell, T. Kaneko, R. Hatakeyama, Measurement of the energy distribution of trapped and free electrons in a current-free double layer. Phys. Plasmas **14**(11), 114503-1–4 (2007)
K. Takahashi, C. Charles, R.W. Boswell, R. Hatakeyama, Radial characterization of the electron energy distribution in a helicon source terminated by a double layer. Phys. Plasmas **15**(7), 074505-1–4 (2008)
K. Takahashi, K. Oguni, H. Yamada, T. Fujiwara, Ion acceleration in a solenoid-free plasma expanded by permanent magnets. Phys. Plasmas **15**(8), 084501-1–4 (2008)
K. Takahashi, C. Charles, R.W. Boswell, W. Cox, R. Hatakeyama, Transport of energetic electrons in a magnetically expanding helicon double layer plasma. Appl. Phys. Lett. **94**(19), 191503-1–3 (2009)

K. Takahashi, Y. Shida, T. Fujiwara, K. Oguni, Supersonic ion beam driven by permanent-magnets-induced double layer in an expanding plasma. IEEE Trans. Plasma Sci. **37**(8), 1532–1536 (2009)
K. Takahashi, Y. Igarashi, T. Fujiwara, Plane and hemispherical potential structures in magnetically expanding plasmas. Appl. Phys. Lett. **97**(4), 041501-1–3 (2010)
K. Takahashi, C. Charles, R.W. Boswell, T. Fujiwara, Double-layer ion acceleration triggered by ion magnetization in expanding radiofrequency plasma sources. Appl. Phys. Lett. **97**(14), 141503-1–3 (2010)
K. Takahashi, Y. Shida, T. Fujiwara, Magnetic-field-induced enhancement of ion beam energy in a magnetically expanding plasma using permanent magnets. Plasma Sources Sci. Technol. **19**(2), 025004-1–7 (2010)
K. Takahashi, C. Charles, R. Boswell, M.A. Lieberman, R. Hatakeyama, Characterization of the temperature of free electrons diffusing from a magnetically expandig current-free double layer plasma. J. Phys. D: Appl. Phys. **43**(16), 162001-1–4 (2010)
K. Takahashi, Y. Itoh, T. Fujiwara, Operation of a permanent-magnets-expanding plasma source connected to a large-volume diffusion chamber. J. Phys. D: Appl. Phys. **44**(1), 015204-1–5 (2011)
K. Takahashi, C. Charles, R.W. Boswell, T. Fujiwara, Electron energy distribution of a current-free double layer: Druyvesteyn theory and experiments. Phys. Rev. Lett. **107**(3), 035002-1–4 (2011)
K. Takahashi, T. Lafleur, C. Charles, P. Alexander, R.W. Boswell, M. Perren, R. Laine, S. Pottinger, V. Lappas, T. Harle, D. Lamprou, Direct thrust measurement of a permanent magnet helicon double layer thruster. Appl. Phys. Lett. **98**(14), 141503-1–3 (2011a)
K. Takahashi, T. Lafleur, C. Charles, P. Alexander, R.W. Boswell, Electron diamagnetic effect on axial force in an expanding plasma: experiments and theory. Phys. Rev. Lett. **107**(23), 235001-1–4 (2011b)
K. Takahashi, T. Lafleur, C. Charles, P. Alexander, R.W. Boswell, Axial force imparted by a current-free magnetically expanding plasma. Phys. Plasmas **19**(8), 083509-1–8 (2012)
K. Takahashi, D. Sato, K. Takaki, A. Ando, Development of a compact magnetically expanding plasma source with a strong magnetic field. Plasma Sources Sci. Technol. **22**(5), 055002-1–5 (2013)
K. Takahashi, C. Charles, R.W. Boswell, Approaching the theoretical limit of diamagnetic-induced momentum in a rapidly diverging magnetic nozzle. Phys. Rev. Lett. **110**(19), 195003-1–5 (2013a)
K. Takahashi, C. Charles, R.W. Boswell, A. Ando, Performance improvement of a permanent magnet helicon plasma thruster. J. Phys. D: Appl. Phys. **46**(35), 352001-1–5 (2013b)
K. Takahashi, C. Charles, R.W. Boswell, A. Ando, Effect of magnetic and physical nozzles on plasma thruster performance. Plasma Sources Sci. Technol. **23**(4), 044004-1–9 (2014)
K. Takahashi, A. Komuro, A. Ando, Low-pressure, high-density, and supersonic plasma flow generated by a helicon magnetoplasmadynamic thruster. Appl. Phys. Lett. **105**(19), 193503-1–4 (2014)
K. Takahashi, A. Chiba, A. Ando, Modifications of wave and plasma structures by a mechanical aperture in a helicon plasma thruster. Plasma Sources Sci. Technol. **23**(6), 064005-1–9 (2014)
K. Takahashi, A. Chiba, A. Komuro, A. Ando, Axial momentum lost to a lateral wall of a helicon plasma source. Phys. Rev. Lett. **114**(19), 195001-1–5 (2015)
K. Takahashi, A. Komuro, A. Ando, Effect of source diameter on helicon plasma thruster performance and its high power operation. Plasma Sources Sci. Technol. **24**(5), 055004-1–8 (2015)
K. Takahashi, A. Komuro, A. Ando, Measurement of plasma momentum exerted on target by a small helicon plasma thruster and comparison with direct thrust measurement. Rev. Sci. Instrum. **86**(2), 023505-1–6 (2015)
K. Takahashi, A. Komuro, A. Ando, Operating a magnetic nozzle helicon thruster with strong magnetic field. Phys. Plasmas **23**(3), 033505-1–7 (2016)
K. Takahashi, A. Chiba, A. Komuro, A. Ando, Experimental identification of an azimuthal current in a magnetic nozzle of a radiofrequency plasma thruster, Plasma Sources Sci. Technol. Plasma Sources Sci. Technol. **25**(5), 055011-1–8 (2016)
K. Takahashi, Y. Takao, A. Ando, Neutral-depletion-induced axially asymmetric density in a helicon source and imparted thrust. Appl. Phys. Lett. **108**(7), 074103-1–4 (2016)
K. Takahashi, Y. Takao, A. Ando, Modifications of plasma density profile and thrust by neutral injection in a helicon plasma thruster. Appl. Phys. Lett. **109**(19), 194101-1–4 (2016)
K. Takahashi, S. Takayama, A. Komuro, A. Ando, Standing helicon wave induced by a rapidly bent magnetic field in plasmas. Phys. Rev. Lett. **116**(13), 135001-1–5 (2016)
K. Takahashi, H. Akahoshi, C. Charles, R.W. Boswell, A. Ando, High temperature electrons exhausted from rf plasma sources along a magnetic nozzle. Phys. Plasmas **24**(8), 084503-1–4 (2017)

K. Takahashi, Y. Nakano, A. Ando, Frequency-tuning radiofrequency plasma source operated in inductively-coupled mode under a low magnetic field. J. Phys. D: Appl. Phys. **50**(26), 265201-1–6 (2017)
K. Takahashi, Y. Takao, A. Ando, Thrust imparted by a stepped-diameter magnetic nozzle rf plasma thruster. Appl. Phys. Lett. **113**(3), 034101-1–4 (2018)
K. Takahashi, C. Charles, R.W. Boswell, A. Ando, Adiabatic expansion of electron gas in a magnetic nozzle. Phys. Rev. Lett. **120**(4), 045001-1–5 (2018)
K. Takahashi, C. Charles, R.W. Boswell, A. Ando, Demonstrating a new technology for space debris removal using a bi-directional plasma thruster. Sci. Rep. **8**, 14417-1–10 (2018)
K. Takahashi, T. Sugawara, H. Akahoshi, Y. Takao, A. Ando, Development of a momentum vector measurement instrument in steady-state plasmas. AIP Adv. **8**(10), 105117-1–10 (2018)
Y. Takao, K. Takahashi, Numerical validation of axial momentum lost to a lateral wall induced by neutral depletion. Phys. Plasmas **22**(11), 113509-1–6 (2015)
K. Takase, K. Takahashi, Y. Takao, Effects of neutral distribution and external magnetic field on plasma momentum in electrodeless plasma thrusters. Phys. Plasmas **25**(2), 023507-1–8 (2018)
K. Terasaka, S. Yoshimura, K. Ogiwara, M. Aramaki, M.Y. Tanaka, Experimental studies on ion acceleration and stream line detachment in a diverging magnetic field. Phys. Plasmas **17**(7), 072106-1–6 (2010)
K. Terasaka, S. Yoshimura, K. Ogiwara, M. Aramaki, M.Y. Tanaka, Observation of ion stream line detachment and onset of azimuthal rotation in a diverging magnetic field. IEEE Trans. Plasma Sci. **39**(11), 2470–2471 (2011)
S.C. Thakur, Z. Harvery, I.A. Biloiu, A. Hansen, R.A. Hardin, W.S. Przybysz, E.E. Scime, Increased upstream ionization due to formation of a double layer. Phys. Rev. Lett. **102**(3), 035004-1–4 (2009)
B. Tian, M. Merino, E. Ahedo, Two-dimensional plasma-wave interaction in an helicon plasma thruster with magnetic nozzle. Plasma Sources Sci. Techno. **27**(11), 114003-1–12 (2018)
H. Tobari, A. Ando, M. Inutake, K. Hattori, Characteristics of electromagnetically accelerated plasma flow in an externally applied magnetic field. Phys. Plasmas **14**(9), 093507-1–10 (2007)
S. Tonooka, I. Funaki, T. Matsuoka, S. Iwabuchi, T. Nakamura, S. Shinohara, H. Nishida. Presented at joint conference of 30th international symposium on space technology and science, 34th international electric propulsion conference, and 6th Nano-satellite symposium, Hyogo-Kobe, Japan. IEPC-2015-413 / ISTS-2015-b-413 (2015)
F. Trezzolani, M. Manente, A. Selmo, D. Melazzi, M. Magarotto, D. Moretto, P. de Carlo, M. Pessana, D. Pavarin, Development and test of an high power RF plasma thruster in project SAPERE-STRONG. Presented at The 35th international electric propulsion conference, Atlanta, Georgia, USA. IEPC-2017-462 (2017)
F. Trezzolani, M. Manente, E. Toson, A. Selmo, M. Magarotto, D. Moretto, F. Bos, P. De Carlo, D. Melazzi, D. Pavarin, Development and testing of a miniature helicon plasma thruster. Presented at the 35th international electric propulsion conference, Atlanta, Georgia, USA. IEPC-2017-519 (2017)
A. Usadi, A. Kageyama, K. Watanabe, T. Sato, A global simulation of the magnetosphere with a long tail: southward and northward interplanetary magnetic field. J. Geophys. Res. **98**(A5), 7503–7517 (1993)
V.F. Virko, Y.V. Virko, V.M. Slobodyan, K.P. Shamrai, The effect of magnetic configuration on ion acceleration from a compact helicon source with permanent magnets. Plasma Sources Sci. Technol. **19**(1), 015004-1–7 (2010)
V.N. Volynets, W. Park, Y.N. Tolmachev, V.G. Pashkovsky, J. Yoo, Spatial variation of plasma parameters and ion acceleration in an inductive plasma system. J. Appl. Phys. **99**(4), 043302-1–5 (2006)
M.D. West, C. Charles, R.W. Boswell, A high sensitivity momentum flux measuring instrument for plasma thruster exhausts and diffusive plasmas. Rev. Sci. Instrum. **80**(5), 053509-1–9 (2009)
M.D. West, C. Charles, R.W. Boswell, Operating radio frequency antennas immersed in vacuum: implications for ground-testing plasma thrusters. J. Propul. Power **26**(4), 892–896 (2010)
M. Wiebold, Y. Sung, J.E. Scharer, Experimental observation of ion beams in the Madison Helicon eXperiment. Phys. Plasmas **18**(6), 063501-1–10 (2011)
L.T. Williams, M.L.R. Walker, Thrust measurements of a radio frequency plasma source. J. Propul. Power **29**(3), 520–527 (2013)
R. Winglee, T. Ziemba, L. Giersch, J. Prager, J. Carscadden, B.R. Roberson, Simulation and laboratory validation of magnetic nozzle effects for the high power helicon thruster. Phys. Plasmas **14**(6), 063501-1–14 (2007)

K.G. Xu, M.L. Walker, High-power, null-type, inverted pendulum thrust stand. Rev. Sci. Instrum. **80**(5), 055103-1–6 (2009)

S. Yun, K. Taylor, G.R. Tynan, Measurement of radial neutral pressure and plasma density profiles in various plasma conditions in large-area high-density plasma sources. Phys. Plasmas **7**(8), 3448–3456 (2000)

Y. Zhang, C. Charles, R. Boswell, Thermodynamic study on plasma expansion along a divergent magnetic field. Phys. Rev. Lett. **116**(2), 025001-1–5 (2016)

Y. Zhang, C. Charles, R.W. Boswell, A polytropic model for space and laboratory plasmas described by bi-Maxwellian electron distributions. Astrophys. J. **829**(1), 10-1–5 (2016)

T. Ziemba, P. Euripides, J. Slough, R. Winglee, L. Giersch, J. Carscadden, T. Schnackenberg, S. Isley, Plasma Sources Sci. Technol. **15**(3), 517–525 (2006)

M. Zuin, R. Cavazzana, E. Martines, G. Serianni, V. Antoni, M. Bagatin, M. Andrenucci, F. Paganucci, P. Rossetti, Kink instability in applied-field magnetoplasmadynamic thrusters. Phys. Rev. Lett. **92**(22), 225003-1–4 (2004)